Memoirs of the Faculty of Engineering, Nagoya University
Vol. 39, No. 2 (1987)

THERMOGASDYNAMICS OF HYPERVELOCITY VEHICLE

TOSHI FUJIWARA, KAZUHIRO HORIE, K. V. REDDY
and KAZUMI MASUDA

Department of Aeronautical Engineering

(Received October 31, 1987)

Part I.
TWO-DIMENSIONAL HYPERSONIC FLOWS INCLUDING CHEMICAL REACTION

TOSHI FUJIWARA, KAZUHIRO HORIE, and KAZUMI MASUDA

Abstract

Two-dimensional hypersonic flows of the order of Mach number 25 are numerically solved for a blunt-body configuration using the Euler equations. The utilized numerical fluid dynamics technique is the Beam-Warming finite difference one, where a bow shock wave in front of the blunt body is successfully captured in terms of several grid points, along with a mixed flow shock layer consisting of supersonic and subsonic regions separated by a sonic line. Starting from a simple set of chemical reactions involved in the dissociation and ionization of oxygen and nitrogen molecules, the numerical analysis proceeded to a fairly complicated reaction system where a total of 17 reactions and 11 chemical species are included.

The results show that the Beam-Warming technique gives convergence to extremely fast hypersonic steady flow problems, even if there are complicated chemical reactions that might cause serious stiffness difficulties. However, even the present less stiff flow fields suffered consistent oscillations in the process of convergence to steady solutions. The difficulties were controlled by adjusting the second-order and fourth-order artificial viscosities and the local time step.

The acquired shapes of a bow shock wave and a sonic line showed good agreements with existing theories and experimental results.

Introduction

The detached shock wave and downstream ultra-high-temperature flow around a two-dimensional semicircle-straight-body configuration are solved applying the Beam-Warming technique to the Euler equations. Since the incoming flow Mach number is assumed 25.2, the Rankine-Hugoniot relations give the temperature ratio

128, pressure ratio 750 and density ratio 6 across the normal portion of the shock wave for $\gamma=1.4$.

The purpose of the study is to incorporate a number of elementary chemical reactions, including the chemical species N_2, O_2, N_2^+, O_2^+, N, O, N^+, O^+, e, NO and NO^+, into a shock capturing technique (Beam-Warming) and to try to eliminate stiffness (existence of multi time scales having different orders of magnitude) in the source terms of the Euler equations.

In principle, the stiffness can be mitigated or in some cases completely eliminated by applying implicit schemes to handle source terms corresponding to chemical reaction. Depending upon the extent of implicitness, a scheme can be called fully implicit (the entire equations are solved implicitly), semi-implicit (only the source terms are handled implicitly) or explicit (the equations are solved entirely explicitly). A typical example of such distinctions is shown in the TVD analyses of Yee.[1] A different version of TVD, i. e. the explicit FCT technique[2] is successfully applied to a number of chemically reacting flows, typically 2-dimensional nonsteady gaseous detonation problems.[3]

Another attempt to avoid the stiffness would be utilization of the steady-state approximation or partial equilibrium to certain chemical species: A criterion to use the steady-state approximation is the concentration of the species to be extremely low throughout the calculation: this is easily detected by monitoring the signs of the concentration and its rate of mass production (naturally, the concentration must remain always positive from its physical character, while the stiffness often causes the concentration negative).

Stiffness is challenged also by mixing several different methods; for example, a finite difference technique accompanied by a Fourier/Chebychev spectral method where the source terms of chemical reaction are approximated using 4th-order Runge-Kutta expressions.[4]

Out of numerous real gas effects, the present model accounts for (i) initially 3 and (ii) later 17 sets of elementary reactions, the rate constants of which are acquired from each forward reaction rate and its associated equilibrium constant as given functions of temperature in the temperature range under consideration. The enthalpy and the gas constant are assumed to be weighted functions of concentrations only as a result of different molecular weights in the gas mixture, and therefore the specific heat ratio γ is not a constant.

In order to obtain a good stability and a rapid convergence to a steady solution, the choice of second-order as well as fourth-order artificial viscosities and local time is performed carefully as shown in a typical example:

Step Number	Local Time	Artificial Viscosities		
(N)	$(\Delta\tau)_{ref}$	κ_2	κ_4	Ω
$0 \sim 2000$	0.25	0.30	0.01	0.1333
$2000 \sim 3000$	0.5	0.30	0.01	0.1333
$3000 \sim 3100$	0.5	0.15	0.01	0.1333
$3100 \sim 3200$	0.5	0.10	0.01	0.1333

After finding out a good combination of the parameters, we kept using nearly identical parameters for different calculations. However, slow convergence or occasionally divergence was observed conceivably due to the coupling between stiffness and large shock thickness.

Chapter 1. A Hypersonic Ideal Gas Flow around a Blunt Body[14]

1. Flow Model and Fundamental Equations

The purpose of this chapter is to obtain the position and shape of a bow shock wave and the subsequent shock layer, when an AOTV (Aero-assisted Orbital Transfer Vehicle) is flying at an altitude about 70 km with a Mach number 25.2.[6] The AOTV is now approximated by a two-dimensional blunt body consisting of a semi-circle-straight-line combination.[5]

The flow is assumed compressible, inviscid, ideal and chemically nonreacting. Treating the gas as continuum flow (the Knudsen number is estimated 10^{-2})[17], the fundamental equations are the Euler equations shown below:

Mass; $$\frac{\partial\bar{\rho}}{\partial\bar{t}}+\frac{\partial(\bar{\rho}\bar{u})}{\partial\bar{x}}+\frac{\partial(\bar{\rho}\bar{v})}{\partial\bar{y}}=0 \tag{1}$$

x-Momentum; $$\frac{\partial\bar{u}}{\partial\bar{t}}+\bar{u}\frac{\partial\bar{u}}{\partial\bar{x}}+\bar{v}\frac{\partial\bar{u}}{\partial\bar{y}}=-\frac{1}{\bar{\rho}}\frac{d\bar{p}}{d\bar{x}} \tag{2}$$

y-Momentum; $$\frac{\partial\bar{v}}{\partial\bar{t}}+\bar{u}\frac{\partial\bar{v}}{\partial\bar{x}}+\bar{v}\frac{\partial\bar{v}}{\partial\bar{y}}=-\frac{1}{\bar{\rho}}\frac{d\bar{p}}{d\bar{y}} \tag{3}$$

Energy; $$\frac{\partial\bar{e}}{\partial\bar{t}}+\frac{\partial[(\bar{e}+\bar{p})\bar{u}]}{\partial\bar{x}}+\frac{\partial[(\bar{e}+\bar{p})\bar{v}]}{\partial\bar{y}}=0 \tag{4}$$

Equation of State; $$\bar{p}=\bar{\rho}\bar{R}\bar{T} \tag{5}$$

where $\bar{\rho}$ denotes the density, $\bar{p}$ the pressure, $\bar{T}$ the temperature, the total energy

$$\bar{e}=\bar{\rho}\left(\bar{h}+\frac{\bar{w}^2}{2}\right)-\bar{p}, \tag{6}$$

$\bar{h}$ the enthalpy per unit volume, and

$$\bar{w}^2=\bar{u}^2+\bar{v}^2. \tag{7}$$

Here the following non-dimensionalization is introduced:

The velocity in x-direction;	$u=\bar{u}/\bar{w}_\infty$	,
The velocity in y-direction;	$v=\bar{v}/\bar{w}_\infty$	,
x-coordinate;	$x=\bar{x}/\bar{L}$	,
y-coordinate	$y=\bar{y}/\bar{L}$	,
Temperature;	$T=\bar{T}/(\bar{w}_\infty^2/\bar{c}_v)$	,
Pressure;	$p=\bar{p}/(\bar{\rho}_\infty\bar{w}_\infty^2)$	,
Energy;	$e=\bar{e}/(\bar{\rho}_\infty\bar{w}_\infty^2)$	,
Mass density;	$\rho=\bar{\rho}/\bar{\rho}_\infty$	,
Time;	$t=\bar{t}/(\bar{L}/\bar{w}_\infty)$	.

Using such dimensionless quantities, the four differential equations (1) through (4)

can be written in the following vector form:

$$\frac{\partial U}{\partial t}+\frac{\partial F}{\partial x}+\frac{\partial G}{\partial y}=0 \tag{8}$$

$$U=\begin{pmatrix}\rho\\ \rho u\\ \rho v\\ e\end{pmatrix},\qquad F=\begin{pmatrix}\rho u\\ \rho u^2+p\\ \rho uv\\ (e+p)u\end{pmatrix},\qquad G=\begin{pmatrix}\rho v\\ \rho uv\\ \rho v^2+p\\ (e+p)v\end{pmatrix} \tag{9}$$

The equation of state (5) and the total energy (6) can also be non-dimensionalized as

$$p=(\gamma-1)\rho T, \tag{10}$$

$$e=p/(\gamma-1)+\rho w^2/2, \tag{11}$$

where the specific heat ratio $\gamma=\text{constant}=1.4$.

2. Coordinate Transformation

A transformation is performed from a physical space (x, y) to a computational coordinate (ξ, η) where ξ and η are a uniform-mesh orthogonal system. In general, the transformation is given by the following equations:

$$\begin{aligned}\xi&=\xi\ (x,\ y),\\ \eta&=\eta\ (x,\ y),\end{aligned} \tag{12}$$

the differential transformation of which is given by

$$\begin{pmatrix}\frac{\partial}{\partial x}\\ \frac{\partial}{\partial y}\end{pmatrix}=\begin{pmatrix}\frac{\partial \xi}{\partial x} & \frac{\partial \eta}{\partial x}\\ \frac{\partial \xi}{\partial y} & \frac{\partial \eta}{\partial y}\end{pmatrix}\begin{pmatrix}\frac{\partial}{\partial \xi}\\ \frac{\partial}{\partial \eta}\end{pmatrix}=\begin{pmatrix}\xi_x & \eta_x\\ \xi_y & \eta_y\end{pmatrix}\begin{pmatrix}\frac{\partial}{\partial \xi}\\ \frac{\partial}{\partial \eta}\end{pmatrix}. \tag{13}$$

Thus, the transformation Jacobian is written as

$$J=\xi_x\eta_y-\xi_y\eta_x. \tag{14}$$

On the other hand, the inverse transformation

$$\begin{aligned}x&=x\ (\xi,\ \eta),\\ y&=y\ (\xi,\ \eta),\end{aligned} \tag{15}$$

gives

$$\begin{pmatrix} \frac{\partial}{\partial \xi} \\ \frac{\partial}{\partial \eta} \end{pmatrix} = \begin{pmatrix} \frac{\partial x}{\partial \xi} & \frac{\partial y}{\partial \xi} \\ \frac{\partial x}{\partial \eta} & \frac{\partial y}{\partial \eta} \end{pmatrix} \begin{pmatrix} \frac{\partial}{\partial x} \\ \frac{\partial}{\partial y} \end{pmatrix} = \begin{pmatrix} x_\xi & y_\xi \\ x_\eta & y_\eta \end{pmatrix} \begin{pmatrix} \frac{\partial}{\partial x} \\ \frac{\partial}{\partial y} \end{pmatrix}, \tag{16}$$

and the Jacobian

$$J' = x_\xi y_\eta - x_\eta y_\xi. \tag{17}$$

The inverse matrix of Eq. (16) gives

$$\begin{pmatrix} \frac{\partial}{\partial x} \\ \frac{\partial}{\partial y} \end{pmatrix} = \frac{1}{x_\xi y_\eta - x_\eta y_\xi} \begin{pmatrix} y_\eta & -y_\xi \\ -x_\eta & x_\xi \end{pmatrix} \begin{pmatrix} \frac{\partial}{\partial \xi} \\ \frac{\partial}{\partial \eta} \end{pmatrix}, \tag{18}$$

from which the relation between the two Jacobians is obtained as

$$J = \frac{y_\eta x_\xi - x_\eta y_\xi}{J'^2} = \frac{1}{y_\eta x_\xi - x_\eta y_\xi} = \frac{1}{J'}. \tag{19}$$

The combination of Eqs. (13) and (16) gives

$$\begin{pmatrix} \frac{\partial}{\partial x} \\ \frac{\partial}{\partial y} \end{pmatrix} = \begin{pmatrix} \xi_x & \eta_x \\ \xi_y & \eta_y \end{pmatrix} \begin{pmatrix} x_\xi & y_\xi \\ x_\eta & y_\eta \end{pmatrix} \begin{pmatrix} \frac{\partial}{\partial x} \\ \frac{\partial}{\partial y} \end{pmatrix} \tag{20}$$

from which it is obvious to derive the relation

$$\begin{pmatrix} \xi_x & \eta_x \\ \xi_y & \eta_y \end{pmatrix} \begin{pmatrix} x_\xi & y_\xi \\ x_\eta & y_\eta \end{pmatrix} = \begin{pmatrix} 1 & 0 \\ 0 & 1 \end{pmatrix} \tag{21}$$

and

$$\begin{pmatrix} \xi_x & \eta_x \\ \xi_y & \eta_y \end{pmatrix} = \frac{1}{J'} \begin{pmatrix} y_\eta & -y_\xi \\ -x_\eta & x_\xi \end{pmatrix} \tag{22}$$

Thus the following relations hold:

$$\begin{aligned} \xi_x &= J y_\eta, & \xi_y &= -J x_\eta, \\ \eta_x &= -J y_\xi, & \eta_y &= J x_\xi. \end{aligned} \tag{23}$$

Using Eq. (23), the differentiations are transformed as

$$\frac{\partial}{\partial t} = \frac{\partial}{\partial \tau},$$

$$\frac{\partial}{\partial x}=\xi_x\frac{\partial}{\partial\xi}+\eta_x\frac{\partial}{\partial\eta}=J\left(y_\eta\frac{\partial}{\partial\xi}-y_\xi\frac{\partial}{\partial\eta}\right),$$

$$\frac{\partial}{\partial y}=\xi_y\frac{\partial}{\partial\xi}+\eta_y\frac{\partial}{\partial\eta}=J\left(-x_\eta\frac{\partial}{\partial\xi}+x_\xi\frac{\partial}{\partial\eta}\right). \tag{24}$$

As a result of using Eq. (24). the fundamental equations become of the form

$$\frac{\partial\hat{U}}{\partial t}+\frac{\partial\hat{F}}{\partial\xi}+\frac{\partial\hat{G}}{\partial\eta}=0, \tag{25}$$

where

$$\begin{aligned}\hat{U}&=J^{-1}U,\\ \hat{F}&=y_\eta F-x_\eta G,\\ \hat{G}&=x_\xi G-y_\xi F.\end{aligned} \tag{26}$$

3. Difference Scheme

As a difference scheme, the following Beam-Warming technique is used:[7]

$$\Delta\hat{U}^n=\frac{\theta\Delta\tau}{1+\delta}\frac{\partial}{\partial\tau}\Delta\hat{U}^n+\frac{\Delta\tau}{1+\delta}\frac{\partial}{\partial\tau}\hat{U}^n+\frac{\delta}{1+\delta}\Delta\hat{U}^{n-1}$$
$$+O\left[\left(\theta-\frac{1}{2}-\delta\right)\Delta\tau^2+\Delta\tau^3\right], \tag{27}$$

where

$$\begin{aligned}\hat{U}^n&=\hat{U}(n\Delta\tau),\\ \Delta\hat{U}^n&=\hat{U}^{n+1}-\hat{U}^n,\end{aligned} \tag{28}$$

and θ and δ are arbitrary parameters related with accuracy. Using the Taylor expansion of a difference term in Eq. (27)

$$\Delta\hat{U}^n=\hat{U}^{n+1}-\hat{U}^n=\hat{U}^n+\frac{\partial\hat{U}^n}{\partial\tau}\Delta\tau+\frac{1}{2}\frac{\partial^2\hat{U}^n}{\partial\tau^2}\Delta\tau^2+O(\Delta\tau^3)-\hat{U}^n, \tag{29}$$

Eq. (27) automatically holds for the order of accuracy ($\Delta\tau$), while necessitating the following condition for the order of accuracy ($\Delta\tau^2$):

$$\frac{1}{2}(1+\delta)\frac{\partial^2\hat{U}^n}{\partial\tau^2}-\left(\theta\frac{\partial^2\hat{U}^n}{\partial\tau^2}-\frac{1}{2}\delta\frac{\partial^2\hat{U}^n}{\partial\tau^2}\right)=\left(\delta+\frac{1}{2}-\theta\right)\frac{\partial^2\hat{U}^n}{\partial\tau^2}=0. \tag{30}$$

Thus the Beam-Warming technique is of the second-order accuracy with respect to time only when

$$\delta+\frac{1}{2}-\theta=0. \tag{31}$$

Note in Eq. (34) that $\hat{A}$ and $\hat{B}$ are defined as

$$\hat{A}=\frac{\partial \hat{F}}{\partial \hat{U}}=\frac{\partial(y_\eta F-x_\eta G)}{J^{-1}\partial U}=J(y_\eta A-x_\eta B),$$
$$\hat{B}=\frac{\partial \hat{G}}{\partial \hat{U}}=\frac{\partial(-y_\xi F+x_\xi G)}{J^{-1}\partial U}=J(-y_\xi A+x_\xi B). \tag{32}$$

In the present calculation, the selected parameters are

$$\theta=1, \quad \delta=\frac{1}{2}. \tag{33}$$

The final Beam-Warming expression of the fundamental equation (25) reduces to the following factorized form:

$$\left\{I+\frac{\theta \Delta\tau}{1+\delta}\frac{\partial \hat{A}^n}{\partial \xi}\right\}\left\{I+\frac{\theta \Delta\tau}{1+\delta}\frac{\partial \hat{B}^n}{\partial \eta}\right\}\Delta \hat{U}^n$$
$$=-\frac{\Delta\tau}{1+\delta}\left(\frac{\partial \hat{F}^n}{\partial \xi}+\frac{\partial \hat{G}^n}{\partial \eta}\right)+\frac{\delta}{1+\delta}\Delta \hat{U}^{n-1}+O\left[\left(\delta-\theta+\frac{1}{2}\right)\Delta\tau^2+\Delta\tau^3\right] \tag{34}$$

To improve the convergence characters of the scheme (34), the following artificial viscosities are added to the both-hand sides of Eq. (34):
(i) A second-order artificial viscosity to the implicit side;

$$-(\Omega J^{-1}\Delta\nabla J)\Delta \hat{U}^n. \tag{35}$$

(ii) Second- and fourth-order artificial viscosities to the explicit side[8,15,16];

$$\nabla(\sigma_{j+1}{J_{j+1}}^{-1}+\sigma_j {J_j}^{-1})(\varepsilon^{(2)}\Delta \hat{U}^n-\varepsilon^{(4)}\Delta\nabla\Delta \hat{U}^n), \tag{36}$$

where the constants are defined as

$$\varepsilon^{(2)}=\kappa_2\Delta\tau f\ (\gamma_{j+1}, \gamma_j, \gamma_{j-1}),$$
$$\varepsilon^{(4)}=\max\ (0, \kappa_4\Delta\tau-\varepsilon^{(2)}),$$
$$\sigma=J\,|\,y_\eta u-x_\eta v\,|+a\sqrt{\xi_x^2+\xi_y^2}+J\,|\,x_\xi v-y_\eta u\,|+a\sqrt{\eta_x^2+\eta_y^2}, \tag{37}$$
$$\gamma_j=|\,P_{j+1}-2P_j+P_{j-1}\,|\,/\,|\,P_{j+1}+2P_j+P_{j-1}|,$$

while Ω is given from the stability condition by

$$\Omega=\alpha(1+2\delta)/4(1+\delta). \tag{38}$$

A typical example on the present choice of the parameters is

$$\kappa_2=0.15, \ \kappa_4=0.01, \ \alpha=0.4. \tag{39}$$

Inclusion of the fourth-order artificial viscosity in the explicit side increased the

thickness of the bow shock wave in front of a blunt body and yet supressed the Gibbs phenomena on both sides of the shock wave and associated divergence of the calculation.

As a time step of integration, a concept of local time step is introduced here, since the present calculation aims at a steady solution[8,15,16]:

$$\Delta\tau_{\text{local}}=\frac{\Delta\tau_{\text{ref}}}{\sigma}. \tag{40}$$

Using this local time step, the coarse-grid region remote from the blunt body showed a rapid convergence which improved the convergence character of the fine-grid region, and eventually the step numbers to reach a final steady solution is greatly reduced. In addition, the stability of calculation is enhanced as a whole.

The difference equation (34) containing the artificial viscosities in Eqs. (35) and (36) is a simultaneous algebraic equation with regard to the change of dependent variables ΔU. When the spatial differentials are given by second-order central differences, the resulting equations become of the following simultaneous algebraic form:

$$\begin{pmatrix} B_1 & C_1 & & & & \\ A_2 & B_2 & C_2 & & & \\ & \ddots & \ddots & \ddots & & \\ & & & A_{n-1} & B_{n-1} & C_{n-1} \\ & & & & A_n & B_n \end{pmatrix} \begin{pmatrix} u_1 \\ u_2 \\ \vdots \\ u_{n-1} \\ u_n \end{pmatrix} = \begin{pmatrix} D_1 \\ D_2 \\ \vdots \\ D_{n-1} \\ D_n \end{pmatrix} \tag{41}$$

where the coefficient matrix is of a tri-diagonal form. After rewriting, we have

$$\begin{pmatrix} I & B_1^{-1}C_1 & & & & \\ A_2 & B_2 & C_2 & & & \\ & \ddots & \ddots & \ddots & & \\ & & & A_{n-1} & B_{n-1} & C_{n-1} \\ & & & & A_n & B_n \end{pmatrix} \begin{pmatrix} u_1 \\ u_2 \\ \vdots \\ u_{n-1} \\ u_n \end{pmatrix} = \begin{pmatrix} B_1^{-1}D_1 \\ D_2 \\ \vdots \\ D_{n-1} \\ D_n \end{pmatrix}, \tag{42}$$

which, after defining $C_1'=C_1B_1^{-1}$, $D_1'=D_1B_1^{-1}$, is reduced to

$$\begin{pmatrix} I & C_1' & & & \\ O & B_2-A_2C_1' & C_2 & & \\ & \ddots & \ddots & \ddots & \\ & & A_{n-1} & B_{n-1} & C_{n-1} \\ & & & A_n & B_n \end{pmatrix} \begin{pmatrix} u_1 \\ u_2 \\ \vdots \\ u_{n-1} \\ u_n \end{pmatrix} = \begin{pmatrix} B_1^{-1}D_1 \\ D_2 \\ \vdots \\ D_{n-1} \\ D_n \end{pmatrix}. \tag{43}$$

Defining the quantities

$$\begin{aligned} C_k' &= (B_k - A_kC_{k-1}')^{-1}C_k, \\ D_k' &= (D_k - A_kD_{k-1}')(B_k - A_kC_{k-1}'), \end{aligned} \tag{44}$$

we finally reach the following matrix equation

$$\begin{pmatrix} I & C_1' & & & \\ 0 & I & C_2' & & O \\ & \ddots & \ddots & \ddots & \\ & & 0 & I & C_{n-1}' \\ & O & & 0 & I \end{pmatrix} \begin{pmatrix} u_1 \\ u_2 \\ \vdots \\ u_{n-1} \\ u_n \end{pmatrix} = \begin{pmatrix} D_1' \\ D_2' \\ \vdots \\ D_{n-1}' \\ D_n' \end{pmatrix}, \tag{45}$$

from which we have

$$\begin{aligned} u_k + C_k'u_{k+1} &= D_k' \quad (1 \leqq k \leqq m-1), \\ u_m &= D_m'. \end{aligned} \tag{46}$$

Using the above-mentioned technique, the ξ-direction and the η-direction are solved respectively; the obtained $\Delta\hat{U}^n$ gives the dependent variable vector U^{n+1} at the next time step $(n+1)$:

$$U^{n+1} = U^n + J\Delta\hat{U}^n. \tag{47}$$

4. Utilized Grids

A typical example of the grid system utilized in the calculation is shown in Fig. 1. With regard to the grid generation, the following respects are taken into account:

(i) Grid lines are formed algebraically; an η = constant line is an ellipse plus a straight line, while a ξ = constant line is orthogonal to the η = constant lines.
(ii) An η = constant line is chosen to nearly agree with a bow shock wave; this is because the boundary conditions are easy to impose in the downstream and in addition the location of the bow shock wave is more accurately determined.
(iii) More grid points are clustered in the regions where the flow is expected to have higher gradients; in other words, near the body tip and the merging point of ellipse and straight line.
(iv) Grids are also clustered near the body surface and the outflow boundary in the calculated domain, because the extrapolation boundary conditions could cause large errors, resulting in the occurrence of physically non-permissible conditions.

5. Initial Conditions

The flow conditions are very simple. A uniform flow is steadily flowing around a two-dimensional blunt body at a Mach number 25.2, corresponding to the entry into the earth atmosphere at an altitude 70 km. According to the standard atmosphere, the physical conditions at 70 km are approximated as:

$$\begin{aligned} &\text{The density;} && \rho_\infty = 8.73\times10^{-8} && \text{g/cm}^3, \\ &\text{the pressure;} && p_\infty = 55.2 && \text{dyne/cm}^2, \\ &\text{the temperature;} && T_\infty = 219.7 && K. \end{aligned} \tag{48}$$

Since we try to acquire a steady solution using the present nonsteady time-dependent equations, the solution is reached when a flow started from an entirely uniform condition showed a convergence to an unvarying flowfield after a certain number of computational steps. Initially, a bow shock wave is formed at the very proximity of a blunt body surface, due to the collision of an extremely high-Mach-number flow at $t=0$. This bow shock wave develops and moves back to the upstream direction to give an appropriate value to the shock standoff distance. However, the bow shock wave goes too far from the body surface due to the inertial motion, and therefore bounces back to the downstream direction. Such oscillation process continues with its amplitude decaying rapidly, eventually yielding a steady state. This is what we intend to perform in the present problem.

6. Boundary Conditions

In the present problem shown in Fig. 1, the boundaries to the calculation domain consist of the following three regions:
(i) Inflow boundary:
Along an outermost η = constant line, the flow is considered always uniform.
(ii) Outflow boundary:
Since the flow is supersonic everywhere in this region due to the character of our fundamental equations (Euler), the dependent variables are obtained by the

extrapolation from the three upstream points.
(iii) On the body surface:
(iii-a) Velocity boundary condition.

The coordinate transformation gives the relation between the Cartesian velocities (u, v) and the velocities ($\hat{u}$, $\hat{v}$) in the transformed plane:

$$\begin{pmatrix} \hat{u} \\ \hat{v} \end{pmatrix} = J \begin{pmatrix} y_\eta & -x_\eta \\ -y_\xi & x_\eta \end{pmatrix} \begin{pmatrix} u \\ v \end{pmatrix}. \tag{49}$$

The following condition obviously holds on the body surface:

$$\hat{v}_1 = 0. \tag{50}$$

Thus, we have

$$\begin{aligned} & J_1(-y_\xi u + x_\xi v)_1 = 0, \\ \therefore \quad & v_1 = (y_\xi / x_\xi) u_1. \end{aligned} \tag{51}$$

On the other hand, $\hat{u}_1$ is derived from Eq. (49) as

$$\hat{u}_1 = J_1(y_\eta u_1 - x_\eta v_1), \tag{52}$$

which is rewritten using Eq. (51) as

$$\hat{u}_1 = \frac{J_1}{x_\xi}(y_\eta x_\xi - x_\eta y_\xi) u_1 = \frac{u_1}{x_\xi}. \tag{53}$$

Thus we obtain

$$u_1 = x_\xi \hat{u}_1. \tag{54}$$

With regards to v, we obtain likewise

$$\hat{u}_1 = \frac{J_1}{y_\xi}(x_\xi y_\eta - y_\xi x_\eta) v_1 = \frac{v_1}{y_\xi}, \tag{55}$$

yielding

$$v_1 = y_\xi \hat{u}_1. \tag{56}$$

Note here that the required $\hat{u}_1$ can be calculated by the linear extrapolation from the upper three points.
(iii-b) Pressure boundary condition.

Taking the inner product of the fundamental equations (34) and a vector $\vec{N} = (0, -y_\xi, x_\xi, 0)$, we obtain

$$\vec{N} \cdot \left(\frac{\partial \hat{U}}{\partial \tau} + \frac{\partial \hat{F}}{\partial \xi} + \frac{\partial \hat{G}}{\partial \eta} \right) = 0 \tag{57}$$

each term of which is evaluated as:
The first term;

$$\vec{N}\cdot\frac{\partial\hat{U}}{\partial\tau}=-y_\xi\frac{\partial(J^{-1}\rho u)}{\partial\tau}+x_\xi\frac{\partial(J^{-1}\rho v)}{\partial\tau}$$

$$=-\frac{\partial[J^{-1}\rho(-y_\xi u+x_\xi v)]}{\partial\tau}+J^{-1}\rho\left[-u\frac{\partial}{\partial\tau}\left(-\frac{1}{J}\eta_x\right)+v\frac{\partial}{\partial\tau}\left(\frac{1}{J}\eta_y\right)\right]$$

$$=\frac{\partial(J^{-1}\rho J^{-1}\hat{v})}{\partial\tau}+J^{-2}\rho\left(u\frac{\partial\hat{v}}{\partial x}+v\frac{\partial\hat{v}}{\partial y}\right) \tag{58}$$

$$=0\ \text{(because}\ \hat{v}=0).$$

The second term is rewritten as

$$\vec{N}\cdot\frac{\partial\hat{F}}{\partial\hat{\xi}}=-y_\xi\frac{\partial[J^{-1}\rho u\hat{u}+y_\eta P]}{\partial\hat{\xi}}+x_\xi\frac{\partial[J^{-1}\rho v\hat{u}-x_\eta P]}{\partial\hat{\xi}}$$

$$=(y_\xi u+x_\xi v)\frac{\partial(J^{-1}\rho\hat{u})}{\partial\hat{\xi}}+J^{-1}\left(-y_\xi\rho\hat{u}\frac{\partial u}{\partial\hat{\xi}}+x_\xi\rho\hat{u}\frac{\partial v}{\partial\hat{\xi}}\right)$$

$$-y_\xi(y_{\xi\eta}P+y_\eta P_\xi)-x_\xi(x_{\xi\eta}P+x_\eta P_\xi) \tag{59}$$

$$=J^{-1}\hat{v}\frac{\partial(J^{-1}\rho\hat{u})}{\partial\hat{\xi}}+J^{-1}\rho\hat{u}(-y_\xi u_\xi+x_\xi v_\xi)$$

$$-(y_\xi y_\eta+x_\xi x_\eta)P_\xi-(y_\xi y_{\xi\eta}+x_\xi x_{\xi\eta})P$$

The third term is again explicitly written as

$$\vec{N}\cdot\frac{\partial\hat{G}}{\partial\eta}=-y_\xi\frac{\partial(J^{-1}\rho u\hat{v}-y_\xi P)}{\partial\eta}+x_\xi\frac{\partial(J^{-1}\rho v\hat{v}+x_\xi P)}{\partial\eta}$$

$$=(-y_\xi u+x_\xi v)\frac{\partial(J^{-1}\rho\hat{v})}{\partial\eta}+J^{-1}\rho\hat{v}\left(-y_\xi\frac{\partial u}{\partial\eta}+x_\xi\frac{\partial v}{\partial\eta}\right)$$

$$+y_\xi(y_{\xi\eta}P+y_\xi P_\eta)+x_\xi(x_{\xi\eta}P+x_\xi P_\eta) \tag{60}$$

$$=J^{-1}\hat{v}\frac{\partial(J^{-1}\rho\hat{v})}{\partial\eta}+J^{-1}\rho\hat{v}(-y_\xi u_\eta+x_\xi v_\eta)$$

$$+(x_\xi{}^2+y_\xi{}^2)P_\eta+(y_{\xi\eta}y_\xi+x_{\xi\eta}x_\xi)P.$$

The sum of these three terms and the condition $\hat{v}=0$ yield

$$-(y_\xi y_\eta+x_\xi x_\eta)P_\xi+(x_\xi{}^2+y_\xi{}^2)P_\eta=-J^{-1}\rho\hat{u}(-y_\xi u_\xi+x_\xi v_\xi). \tag{61}$$

The pressure on a solid boundary can be evaluated by solving a tridiagonal matrix equation obtained from Eq.(61).

The density on a solid boundary can be determined by linearly extrapolating from the three upper points.

(iii-c) Placing physical limits.

In order to prevent divergence or physically implausible situations to occur during the initial stage of calculation, we have set both upper and lower limits for a certain number of dependent variables, as shown below:

$$\begin{aligned} \rho_{sup} \leqq \rho \leqq \rho_0, \\ e_{sup} \leqq e \leqq e_0, \\ 0 \leqq w \leqq w_{sup}, \end{aligned} \tag{62}$$

where the limits $(\phi)_{sup}$ are the values for a Mach number 1.5 M_∞. The limits with subscript 0 are the stagnation conditions evaluated by the isentropic relations

$$\begin{aligned} \rho_0 &= \rho\left(1+\frac{\gamma-1}{2}M^2\right)^{\frac{1}{\gamma-1}}, \\ p_0 &= p\left(1+\frac{\gamma-1}{2}M^2\right)^{\frac{\gamma}{\gamma-1}}, \\ e_0 &= p_0/(\gamma-1), \end{aligned} \tag{63}$$

and by the Rankine-Hugoniot relations across a shock (upstream x and downstream y)

$$\begin{aligned} M_y^2 &= \left(1+\frac{\gamma-1}{2}M_x^2\right)/\left(\gamma M_x^2-\frac{\gamma-1}{2}\right), \\ \rho_y/\rho_x &= (\gamma+1)M_x^2/[(\gamma-1)M_x^2+2], \\ p_y/p_x &= [1+2\gamma(M_x^2-1)]/(\gamma+1). \end{aligned} \tag{64}$$

7. Results and Discussions on Chemically Nonreacting Flows

A numerical analysis is performed for ideal flows around a blunt body illustrated in Figs. 1 and 12 at an angle of attack zero, with an incoming flow Mach number $M_\infty=3\sim25.2$. Shown below are the results for a Mach number 25.2 which corresponds to the orbital velocity of a low-altitude satellite and therefore is chosen as a typical entry velocity of a spacecraft called AOTV (Aeroassisted Orbital Transfer Vehicle). For reference we list both the jump conditions across a normal shock wave as well as the stagnation conditions for the incoming flow Mach number 25.2:

$$\begin{aligned} p_s/p_\infty &= 741, & p_0/p_\infty &= 818, \\ T_s/T_\infty &= 124, & T_0/T_\infty &= 128, \\ \rho_s/\rho_\infty &= 5.97, & \rho_0/\rho_\infty &= 6.41. \end{aligned} \tag{65}$$

It is noted that as a first step the flow is assumed ideal and nonreacting with $\gamma=1.4$ and therefore there is no real gas effect in the analysis in the present chapter. The flow patterns are shown in Figs. 2 through 4, in terms of iso-pressure, iso-Mach-number and iso-temperature lines. Convergence to a steady state is reached at $N=1600$ steps, by adjusting a local time and the artificial viscosities appearing in the right-hand-side of the Beam-Warming finite difference equation; the utilized convergence criterion is a per-grid residue of ρ less than 10^{-6}.

As shown in the flow patterns, a typical bow shock wave is formed in front

of a two-dimensional blunt body with a certain shock standoff distance. The shock wave is normal and strongest at the stagnation region, and gradually weakens thereafter eventually down to a Mach wave in the far wake region. However, the thickness of the bow shock is already considerably large in the observed domain where we should still be seeing a discontinuous shock. This shock spreading seems to be unavoidable in the Beam-Warming scheme particularly when it is applied to a hypersonic flow.

The reason is attributed to the use of artificial viscosities in the right-hand-side of the Beam-Warming scheme. Due to an enormous jump across a shock wave caused by a hypersonic flow Mach number, a shock wave is always accompanied by strong Gibbs phenomena, generating oscillations during the process of converging to a steady state, leading to divergence. Such oscillations can be suppressed by introducing artificial viscosities of second and fourth orders; however, this in turn causes the thickening of a shock wave unfortunately. Thus, a thick shock wave is considered a tradeoff from stable convergence to a steady solution.

From Figs. 2 through 4, it is possible to know the shock standoff distance and the location of a sonic line. The obtained shock standoff distance, shock shape and sonic line location are compared with the values from other authors in Fig. 25. The calculated shock wave for $M_\infty=25.2$ ($K_2=0.15$, $K_4=0.01$) gives a good agreement with the results obtained by Fuller and Belotserkovskii using a direct method;[9] the present $M=25.2$ result is right between $M_\infty=10$ and ∞. Note, however, that the shock location is defined as a $M=1$ locus out of a number of iso-Mach-number lines within a shock wave.

The distributions of mass density, pressure and temperature along the stagnation streamline are shown in Figs. 5 through 7. With regard to the peaks immediately behind a bow shock wave, we can see a good agreement with the Rankine-Hugoniot relation which is indicated by a horizontal line in each figure.[10] However, we can see the existence of Gibbs phenomena behind a shock wave, most notably in the pressure profile in Fig. 6.

It has been realized after calculation that a finer grid clustered in the shock wave region would have given a thinner shock wave and there is an accuracy problem on the determination of mass density on the body surface; instead of using the present linear extrapolation, a different method having higher order of accuracy should be used.

Chapter 2. Chemically Reacting Flows

1. Introduction

Based on the previous ideal gas calculations, the analysis is upgraded to include a set of elementary reactions corresponding to the dissociation of air molecules (oxygen and nitrogen) and associated endothermicity. As is well known, the realistic elementary reactions that are occurring in the high-temperaure shock layer are categorized into dissociation, exchange reactions, associative ionization and electron impact ionization;[12] a typical example of such a complicated combination of high-temperature reactions associated with hypersonic entry into the earth atmosphere is illustrated in Table 2. Out of these 47 different reactions, only 8 reactions allowing O_2, N_2, O and N are taken into account in the first

Table 1. Set I of the chemical reactions used in the analysis, corresponding to the dissociation of nitrogen and oxygen molecules, where the influence of different collision partners is taken into account.

No. (j)	Chemical reaction	Chemical equilibrium constant term ACE (1)	ACE (2)	ACE (3)	ACE (4)	ACE (5)	Forward reaction rate term ACF (1) : C_j	ACF (2) : ζ_j	ACF (3) : D_j
Dissociation									K
1	$O_2=O+O(M=N)$	2.855	0.988	-6.181	-0.023	-0.001	0.8250E+20	-1.000	59500.0
2	$O_2=O+O(M=O)$	2.855	0.988	-6.181	-0.023	-0.001	0.8250E+20	-1.000	59500.0
3	$O_2=O+O(M=N_2)$	2.855	0.988	-6.181	-0.023	-0.001	0.2750E+20	-1.000	59500.0
4	$O_2=O+O(M=O_2)$	2.855	0.988	-6.181	-0.023	-0.001	0.2750E+20	-1.000	59500.0
5	$N_2=N+N(M=N)$	1.858	-1.325	-9.856	-0.174	0.008	0.1110E+23	-1.600	113200.0
6	$N_2=N+N(M=O)$	1.858	-1.325	-9.856	-0.174	0.008	0.1110E+23	-1.600	113200.0
7	$N_2=N+N(M=N_2)$	1.858	-1.325	-9.856	-0.174	0.008	0.3700E+22	-1.600	113200.0
8	$N_2=N+N(M=O_2)$	1.858	-1.325	-9.856	-0.174	0.008	0.3700E+22	-1.600	113200.0

phase of calculation. Such a simple reaction system, called Set I, is shown in Table 1, while Set II is the most complicated one allowing 5 neutral species N_2, O_2, NO, N, O and their positive ions, along with electron (total 11 species), defined in Table 2. Set III consists of 24 reactions, shown in Table 2 with superscript $*$, eliminating nearly all the ion participating reactions. All the chemical data are taken from Ref. 11.

2. Fundamental Equations of a Chemically Reacting Flow[13,17]

Since the conservation forms remain unchanged for momentum and energy equations even in the presence of chemical reactions, only the equations of species conservation need to be written:

$$\frac{\partial(\bar{\rho}Y_i)}{\partial\bar{t}}+\frac{\partial(\bar{\rho}\bar{u}Y_i)}{\partial\bar{x}}+\frac{\partial(\bar{\rho}\bar{v}Y_i)}{\partial\bar{y}}=\overline{W}_i, \tag{66}$$

where Y_i are the mass fraction of species i and the only non-conservational term $\overline{W}_i$ indicates the rate of mass production of species i. The equation of state is expressed as

$$\bar{p}_i=\bar{\rho}_i\overline{R}_i\overline{T}=\bar{\rho}_i\frac{\overline{R}_0}{\overline{M}_i}\overline{T}, \tag{67}$$

which are summed up with respect to i to give

$$\bar{p}=\bar{\rho}\overline{R}\overline{T}, \tag{68}$$

where the gas constant for a gas mixture is defined as

$$\overline{R}=\overline{R}_0\sum_i (Y_i/\overline{M}_i). \tag{69}$$

Table 2. Set Ⅱ of the chemical reactions involved in the AOTV entry into the earth atmosphere at a hypersonic speed, corresponding to the mechanism of dissociation and ionization of air molecules, where a total of 47 elementary reactions and 11 chemical species are considered.

In Set Ⅱ, the elementary reactions with superscript * are chosen into the calculation, corresponding to the elimination of all but one ion participating reactions.

No.	CHEMICAL REACTION	CHEMICAL EQUILIBRIUM CONSTANT TERM ACE(1)	ACE(2)	ACE(3)	ACE(4)	ACE(5)	FORWARD REACTION RATE TERM ACF(1)	ACF(2)	ACF(3)
	DISSOCIATION								
1*	O2 = O + O (M = N)	2.855	0.988	-6.181	-0.023	-0.001	0.8250E+20	-1.000	59500.0
2*	O2 = O + O (M = O)	2.855	0.988	-6.181	-0.023	-0.001	0.8250E+20	-1.000	59500.0
3*	O2 = O + O (M = N2)	2.855	0.988	-6.181	-0.023	-0.001	0.2750E+20	-1.000	59500.0
4*	O2 = O + O (M = O2)	2.855	0.988	-6.181	-0.023	-0.001	0.2750E+20	-1.000	59500.0
5*	O2 = O + O (M = NO)	2.855	0.988	-6.181	-0.023	-0.001	0.2750E+20	-1.000	59500.0
6	O2 = O + O (M = N+)	2.855	0.988	-6.181	-0.023	-0.001	0.8250E+20	-1.000	59500.0
7	O2 = O + O (M = O+)	2.855	0.988	-6.181	-0.023	-0.001	0.8250E+20	-1.000	59500.0
8	O2 = O + O (M = N2+)	2.855	0.988	-6.181	-0.023	-0.001	0.2750E+20	-1.000	59500.0
9	O2 = O + O (M = O2+)	2.855	0.988	-6.181	-0.023	-0.001	0.2750E+20	-1.000	59500.0
10*	O2 = O + O (M = NO+)	2.855	0.988	-6.181	-0.023	-0.001	0.2750E+20	-1.000	59500.0
11*	O2 = O + O (M = E-)	2.855	0.988	-6.181	-0.023	-0.001	0.1320E+23	-1.000	59500.0
12*	N2 = N + N (M = N)	1.858	-1.325	-9.856	-0.174	0.008	0.1110E+23	-1.600	113200.0
13*	N2 = N + N (M = O)	1.858	-1.325	-9.856	-0.174	0.008	0.1110E+23	-1.600	113200.0
14*	N2 = N + N (M = N2)	1.858	-1.325	-9.856	-0.174	0.008	0.3700E+22	-1.600	113200.0
15*	N2 = N + N (M = O2)	1.858	-1.325	-9.856	-0.174	0.008	0.3700E+22	-1.600	113200.0
16*	N2 = N + N (M = NO)	1.858	-1.325	-9.856	-0.174	0.008	0.3700E+22	-1.600	113200.0
17	N2 = N + N (M = N+)	1.858	-1.325	-9.856	-0.174	0.008	0.1110E+23	-1.600	113200.0
18	N2 = N + N (M = O+)	1.858	-1.325	-9.856	-0.174	0.008	0.1110E+23	-1.600	113200.0
19	N2 = N + N (M = N2+)	1.858	-1.325	-9.856	-0.174	0.008	0.3700E+22	-1.600	113200.0
20	N2 = N + N (M = O2+)	1.858	-1.325	-9.856	-0.174	0.008	0.3700E+22	-1.600	113200.0
21*	N2 = N + N (M = NO+)	1.858	-1.325	-9.856	-0.174	0.008	0.3700E+22	-1.600	113200.0
22*	N2 = N + N (M = E-)	1.858	-1.325	-9.856	-0.174	0.008	0.1110E+25	-1.600	113200.0
23*	NO = N + O (M = N)	0.792	-0.492	-6.761	-0.091	0.004	0.4600E+18	-0.500	75500.0
24*	NO = N + O (M = O)	0.792	-0.492	-6.761	-0.091	0.004	0.4600E+18	-0.500	75500.0
25*	NO = N + O (M = N2)	0.792	-0.492	-6.761	-0.091	0.004	0.2300E+18	-0.500	75500.0
26*	NO = N + O (M = O2)	0.792	-0.492	-6.761	-0.091	0.004	0.2300E+18	-0.500	75500.0
27*	NO = N + O (M = NO)	0.792	-0.492	-6.761	-0.091	0.004	0.2300E+18	-0.500	75500.0
28	NO = N + O (M = N+)	0.792	-0.492	-6.761	-0.091	0.004	0.4600E+18	-0.500	75500.0
29	NO = N + O (M = O+)	0.792	-0.492	-6.761	-0.091	0.004	0.4600E+18	-0.500	75500.0
30	NO = N + O (M = N2+)	0.792	-0.492	-6.761	-0.091	0.004	0.2300E+18	-0.500	75500.0
31	NO = N + O (M = O2+)	0.792	-0.492	-6.761	-0.091	0.004	0.2300E+18	-0.500	75500.0
32*	NO = N + O (M = NO+)	0.792	-0.492	-6.761	-0.091	0.004	0.2300E+18	-0.500	75500.0
33*	NO = N + O (M = E-)	0.792	-0.492	-6.761	-0.091	0.004	0.7360E+20	-0.500	75500.0
	EXCHANGE REACTIONS								
34*	NO + O = N + O2	-2.063	-1.480	-0.580	-0.114	0.005	0.2610E+09	1.290	19220.0
35*	O + N2 = N + NO	1.066	-0.833	-3.095	-0.084	0.004	0.3180E+14	0.100	37700.0
36	O + O2+ = O2 + O+	-0.276	0.038	-2.180	0.055	-0.003	0.6850E+14	-0.520	18600.0
37	N2 + N+ = N + N2+	0.307	-1.076	-0.878	-0.004	-0.001	0.9050E+13	-0.180	12100.0
38	O + NO+ = NO + O+	0.148	-1.011	-4.121	-0.132	0.006	0.2750E+14	0.010	51000.0
39	N2 + O+ = O + N2+	2.979	0.382	-3.237	0.168	-0.009	0.6330E+14	-0.210	22200.0
40	N + NO+ = NO + N+	2.821	0.448	-6.481	0.040	-0.002	0.2210E+16	-0.020	61100.0
41	O2 + NO+ = NO + O2+	0.424	-1.098	-1.941	-0.187	0.009	0.1030E+17	-0.170	32400.0
42	NO+ + N = N2+ + O	2.061	0.204	-4.263	0.119	-0.006	0.1700E+14	0.400	35500.0
	ASSOCIATIVE IONIZATION								
43*	O + N = NO+ + E-	-7.053	-0.532	-4.429	0.150	-0.007	0.1530E+12	-0.370	32000.0
44	O + O = O2+ + E-	-8.692	-3.110	-6.950	-0.151	0.007	0.3850E+12	0.490	80600.0
45	N + N = N2+ + E-	-4.992	-0.328	-8.693	0.269	-0.013	0.1790E+12	0.770	67500.0
	ELECTRON IMPACT IONIZATION								
46	O = O+ + E-	-6.113	-2.035	-15.311	-0.073	0.004	0.3900E+34	-3.780	158500.0
47	N = N+ + E-	-3.441	-0.577	-17.671	0.099	-0.005	0.2500E+35	-3.820	168600.0
1	0.055SEC								

The fundamental equations are non-dimensionalized by introducing the following dimensionless quantities:

$$
\begin{aligned}
&u=\bar{u}/\bar{w}_\infty, \qquad v=\bar{v}/\bar{w}_\infty, \qquad p=\bar{p}/\bar{\rho}_\infty\bar{w}_\infty^2,\\
&x=\bar{x}/\bar{L}, \qquad y=\bar{y}/\bar{L}, \qquad T=\bar{T}/(\bar{w}_\infty^2/\bar{R}_\infty),\\
&R=\bar{R}/\bar{R}_\infty, \quad C_p=\bar{C}_p/\bar{R}_\infty, \quad W_i=\bar{W}_i/(\bar{\rho}_\infty\bar{w}_\infty/\bar{L}),\\
&e=\bar{e}/\bar{\rho}_\infty\bar{w}_\infty^2, \quad \rho=\bar{\rho}/\bar{\rho}_\infty, \qquad t=\bar{t}/(\bar{L}/\bar{w}_\infty),\\
&h=\bar{h}/\bar{w}_\infty^2, \quad M_i\ (\text{molecular weight})=\bar{M}_i/\bar{M}_{air,\infty}.
\end{aligned}
\tag{70}
$$

where $\overline{M}_{air,\infty}$ = molecular weight of incoming uniform flow, and $\overline{R}_\infty$=gas constant of incoming uniform flow.

The fundamental equations are rewritten in the following non-dimensional vector form:

$$\frac{\partial U}{\partial t}+\frac{\partial F}{\partial x}+\frac{\partial G}{\partial y}=W, \tag{71}$$

where the each vector has seven components including four mass densities in the present case, as shown below:

$$U=\begin{pmatrix}\rho_N\\ \rho_O\\ \rho_{N_2}\\ \rho_{O_2}\\ \rho u\\ \rho v\\ e\end{pmatrix},\quad F=\begin{pmatrix}\rho_N u\\ \rho_O u\\ \rho_{N_2}u\\ \rho_{O_2}u\\ \rho u^2+p\\ \rho uv\\ (e+p)u\end{pmatrix},\quad G=\begin{pmatrix}\rho_N v\\ \rho_O v\\ \rho_{N_2}v\\ \rho_{O_2}v\\ \rho uv\\ \rho v^2+p\\ (e+p)v\end{pmatrix},\quad W=\begin{pmatrix}w_N\\ w_O\\ w_{N_2}\\ w_{O_2}\\ 0\\ 0\\ 0\end{pmatrix}, \tag{72}$$

and the equation of state is expressed as

$$p=\rho RT. \tag{73}$$

After the coordinate transformation, Eq. (72) is rewritten as

$$\frac{\partial \hat{U}}{\partial \tau}+\frac{\partial \hat{F}}{\partial \xi}+\frac{\partial \hat{G}}{\partial \eta}=\hat{W}, \tag{74}$$

where the following quantities are defined:

$$\begin{aligned}\hat{U}&=J^{-1}U,\\ \hat{F}&=y_\eta F-x_\eta G,\\ \hat{G}&=x_\xi G-y_\xi F,\\ \hat{W}&=J^{-1}W.\end{aligned} \tag{75}$$

3. Chemical Reactions

As explained in Section 1, the adopted chemical reactions are of three sets (Set I, II and III in Tables 1 and 2). In Set I only the dissociation of molecular oxygen and nitrogen

$$\begin{aligned}&N_2+M \rightleftharpoons N+N+M,\\ &O_2+M \rightleftharpoons O+O+M,\end{aligned} \tag{76}$$

where the third body M is either of the four existing species N_2, O_2, N and O. The rate constant of the forward reaction in Eq. (76-1) is assumed to have a form

$$k_{fj}=C_jT^{\zeta_j}\exp(-D_j/T) \quad \text{in mole-cm-sec-}K\text{ system.} \tag{77}$$

The rate constant of the reverse reaction in Eq. (76-1) is expressed in terms of the concentration equilibrium constant of the reaction and the forward rate constant as

$$k_{rj}=k_{fj}/K_j \tag{78}$$

where the equilibrium constant K_i is a function of the temperature only;

$$K_j=\exp(A_{1j}+A_{2j}\ln Z+A_{3j}Z+A_{4j}Z^2+A_{5j}Z^3),\ Z=10000/T. \tag{79}$$

This equilibrium constant for the reaction (76-1) can easily be constructed by using the species equilibrium constants tabulated in JANAF Tables. The constants appearing in Eqs. (76) and (79) are listed in Tables 1 and 2.[11] Thus, the rate of molar production can be expressed as

$$\begin{aligned}
\frac{d[\mathrm{N}]}{dt}&=2(k_{fm}[\mathrm{N_2}]-k_{rm}[\mathrm{N}]^2)[\mathrm{M}_m],\\
\frac{d[\mathrm{N_2}]}{dt}&=-(k_{fm}[\mathrm{N_2}]-k_{rm}[\mathrm{N}]^2)[\mathrm{M}_m],\\
\frac{d[\mathrm{O}]}{dt}&=2(k_{fl}[\mathrm{O_2}]-k_{rl}[\mathrm{O}]^2)[\mathrm{M}_l],\\
\frac{d[\mathrm{O_2}]}{dt}&=-(k_{fl}[\mathrm{O_2}]-k_{rl}[\mathrm{O}]^2)[\mathrm{M}_m],
\end{aligned} \tag{80}$$

where $l=1\sim4$ and $m=5\sim8$ with respect to the reaction in Table 1.

4. Beam-Warming Difference Scheme for a Chemically Reacting Gas

Applying the Beam-Warming scheme to the fundamental equations (74), we obtain

$$\frac{\partial}{\partial\tau}\Delta\hat{U}^n=\frac{\partial}{\partial\xi}(-\Delta\hat{F})^n+\frac{\partial}{\partial\eta}(-\Delta\hat{G})^n+\Delta\hat{W}^n. \tag{81}$$

Thus, the following difference scheme is reached by treating the source terms explicitly:

$$\begin{aligned}
\Delta\hat{U}^n=&\frac{\theta\Delta\tau}{1+\delta}\left[\frac{\partial}{\partial\xi}(-\Delta\hat{F})^n+\frac{\partial}{\partial\eta}(-\Delta\hat{G})^n+\Delta\hat{W}^n\right]\\
&+\frac{\Delta\tau}{1+\delta}\left[\frac{\partial}{\partial\xi}(-\hat{F})^n+\frac{\partial}{\partial\eta}(-\hat{G})^n+\hat{W}^n\right]+\frac{\delta}{1+\delta}\Delta\hat{U}^{n-1}
\end{aligned}$$

$$+O\left[\left(\theta-\frac{1}{2}-\delta\right)\Delta\tau^2+\Delta\tau^3\right]. \tag{82}$$

We use here the Taylor expansion given by

$$\begin{aligned}
\Delta\hat{F}^n&=\left(\frac{\partial\hat{F}}{\partial\hat{U}}\right)^n\Delta\hat{U}^n+O(\Delta\tau^2)=\hat{A}^n\Delta\hat{U}^n+O(\Delta\tau^2),\\
\Delta\hat{G}^n&=\left(\frac{\partial\hat{G}}{\partial\hat{U}}\right)^n\Delta\hat{U}^n+O(\Delta\tau^2)=\hat{B}^n\Delta\hat{U}^n+O(\Delta\tau^2),\\
\Delta\hat{W}^n&=\left(\frac{\partial\hat{W}}{\partial\hat{U}}\right)^n\Delta\hat{U}^n+O(\Delta\tau^2)=\hat{C}^n\Delta\hat{U}^n+O(\Delta\tau^2),
\end{aligned} \tag{83}$$

where the matrices A, B and C are defined as

$$\begin{aligned}
\hat{A}&=\frac{\partial\hat{F}}{\partial\hat{U}}=J\frac{\partial}{\partial U}(y_\eta F-x_\eta G)=J(y_\eta A-x_\eta B),\\
\hat{B}&=\frac{\partial\hat{G}}{\partial\hat{U}}=J\frac{\partial}{\partial U}(-y_\xi F+x_\xi G)=J(-y_\xi A+x_\xi B),\\
\hat{C}&=\frac{\partial\hat{W}}{\partial\hat{U}}=J\frac{\partial}{\partial U}(J^{-1}W)=\frac{\partial W}{\partial U}=C,
\end{aligned} \tag{84}$$

the details of which are given in Appendix A.

Using Eq. (83), we acquire a difference scheme

$$\begin{aligned}
&\left\{I+\frac{\theta\Delta\tau}{1+\delta}\left[\frac{\partial\hat{A}^n}{\partial\xi}+\frac{\partial\hat{B}^n}{\partial\eta}-\hat{C}^n\right]\right\}\Delta\hat{U}^n\\
&\quad=-\frac{\Delta\tau}{1+\delta}\left[\frac{\partial}{\partial\xi}\hat{F}^n+\frac{\partial}{\partial\eta}\hat{G}^n-\hat{W}^n\right]+\frac{\delta}{1+\delta}\Delta\hat{U}^{n-1}\\
&\qquad+O\left[\left(\theta-\frac{1}{2}-\delta\right)\Delta\tau^2+\Delta\tau^3\right],
\end{aligned} \tag{85}$$

which can be factorized into the final convenient form:

$$\begin{aligned}
&\left\{I+\frac{\theta\Delta\tau}{1+\delta}\left[\frac{\partial\hat{A}^n}{\partial\xi}-\frac{1}{2}\hat{C}^n\right]\right\}\left\{I+\frac{\theta\Delta\tau}{1+\delta}\left[\frac{\partial B^n}{\partial\eta}-\frac{1}{2}\hat{C}^n\right]\right\}\Delta\hat{U}^n\\
&\quad=-\frac{\Delta\tau}{1+\delta}\left[\frac{\partial\hat{F}^n}{\partial\xi}+\frac{\partial\hat{G}^n}{\partial\eta}-\hat{W}^n\right]+\frac{\delta}{1+\delta}\Delta\hat{U}^{n-1}\\
&\qquad+O\left[\left(\theta-\frac{1}{2}-\delta\right)\Delta\tau^2+\Delta\tau^3\right].
\end{aligned} \tag{86}$$

With regard to the artificial viscosities, Eqs. (35) through (39) are used as well. The same expression for a local time step (40) is also used; however, the magnitude of the time step is considerably reduced to overcome the stiffness appearing in chemically reacting flows. $\Delta\tau_{ref}=0.25\sim1.0$ is chosen in the present calculation instead of 1.0.

5. Physico-Chemical Considerations

Since the dependent variable in the energy equation is the energy e in the present formulation, the temperature, the most important physical quantity in a chemically reacting flow, has to be calculated through the process of solving algebraic equations. From the definition of the energy e, we have

$$e+p=\rho\left[\sum_{i=1}^{N} Y_i(C_{pi}T+h_i^0)+\frac{w^2}{2}\right], \tag{87}$$

where the assumption

$$h_i=C_{pi}T+h_i^0 \tag{88}$$

is utilized. h_i^0 denotes the enthalpy of formation of species i. Since the dependent variables e, ρ, w and Y_i are solved, the remaining unknowns turn out to be p and T only, whereas they are related with each other through the equation of state (73). Thus, the final explicit form for the temperature is given as

$$T=\left[e-\rho\left(\sum_{i=1}^{N} Y_i h_i^0+\frac{w^2}{2}\right)\right]/\rho\left[\sum_{i=1}^{N} Y_i C_{pi}-R\right], \tag{89}$$

The utilized grid system is changed from Fig. 1 to Fig. 12.

The initial conditions for a chemically reacting flow is unchanged except for the conditions on the species concentrations. The mass fractions of each species are set in an incoming flow to

$$Y_N=0, \quad Y_O=0, \quad Y_{N_2}=0.7596, \quad Y_{O_2}=0.2404. \tag{90}$$

With regard to the boundary conditions on species concentrations at the exit boundary of the calculation domain, an analysis of characteristics allows linear extrapolation. In order to minimize the error, the grids are clustered in the vicinity of the exit plane, as indicated in Fig. 12. On the other hand, the species concentrations on the wall boundary are specified by the non-catalytic wall boundary condition. Since we are based upon the Euler equations, there is no effect of species diffusion onto the wall boundary. In such a situation, the postulate of no heterogeneous chemical reaction on the wall gives zero gradient on the concentration profile of each species. Thus, the value on the wall is set equal to the upper one.

6. Results and Discussions on Chemically Reacting Flows

The first phase of analysis on chemically reacting flows is performed using Set I chemical reactions shown in Table 1. The obtained results are shown partly in the form of distribution along the stagnation streamline in the shock layer behind a bow shock wave, as shown in Figs. 8 through 11. In fact, the same reaction mechanism Set I is used in extending the computational run from N=3000 to N=3200, while the numerical parameters $\Delta\tau_{\mathrm{ref}}$ and K_2 are altered after N=3000. As illustrated in Fig. 21, the per-grid density residue decreases down to less than 10^{-7}

at N=3000 when we maintain the same parameters. Figs. 8 through 11 are at this instant of good convergence.

In order to decrease the thickness of a bow shock wave the artificial viscosity K_2 is lowered from 0.15 to 0.10 at N=3000 steps, when a sudden jump of the residue is observed in Fig. 21. After a gradual decrease, the residue again increases by the use of a longer local time at N=3100, followed by the decrease less then 10^{-5} at N=3200. Figs. 13 through 20 are at N=3200.

Comparing Figs. 8~11 to each other, we can notice that the chemical reactions greatly change the structure of the shock layer: (i) The shock standoff distance is reduced to about 3/5 of the ideal gas case, as shown in the figures and Fig. 25. (ii) The pressure is seen to be slightly altered, if we compare between Figs. 6 and 9. (iii) In contrast, the density is greatly increased in Fig. 8, while the temperature is much lower than the Rankine-Hugoniot value; this is a result of the equation of state, because the pressure is nearly unchanged as shown in Fig. 9. Why the pressure is unchanged can be explained by the position of a bow shock wave; the shock wave position is determined by the force balance in the shock layer, retaining the pressure at the same level while adjusting the shock standoff distance. On the other hand, the temperature is controlled by the endothermic dissociation of oxygen and nitrogen molecules. Due to the extended thickness of a bow shock caused by the essential character of the Beam-Warming technique and a higher secod-order artificial viscosity $K_2=0.15$, the present shock capturing technique allows chemical reactions to proceed within the otherwise infinitesimally thin shock wave. In other words, the Rankine-Hugoniot relation is not maintained, as seen in Fig. 10, the temperature peak being nearly 1/2 of the R-H value. The doubled density is explained by applying this tendency to the equation of state. The direct effects of chemical reaction are seen in the concentration profile of each species shown in Fig. 11. Oxygen dissociation has completed prior to the arrival at the body surface, and interestingly the mass fraction of equilibrium atomic oxygen remains exactly at the same level as the level of the incoming molecular oxygen, indicating no significant influence of artificial diffusion. Nitrogen dissociation starts later than oxygen and is incomplete even upon arrival at the body surface. This implies that the influence of catalytic recombination of atomic species on the body surface would be overestimated if we assume a fully dissociated flow in the shock layer at the present flight Mach number range $M_\infty=25.2$.

The calculated results will be altered by increasing the local time and reducing the second-order artificial viscosity K_2. The results at N=3200 are shown in Figs. 13~20, where the thickness of a bow shock is hopefully reduced due to a lower artificial viscosity. As typically seen in the distributions along the stagnation streamline in the shock layer of a blunt body, shown in Figs. 17~20, the thickness of a bow shock wave is certainly reduced, leading to a higher peak in the temperature distribution. Chemistry, however, is not significantly altered, giving the same species concentrations on the body surface (stagnation point), as seen in Fig. 20.

The second-phase analysis of a chemically reacting flow is done using Set II chemical reactions (full mechanism) listed in Table 2. Although the calculation is incomplete due to (i) the stiffness caused by the participation of 47 elementary reactions and 11 chemical species, and (ii) a large block tri-diagonal matrix consisting of 14 dependent variables, half-way results are given in Figs. 22 and 23. In order to overcome strong oscillations encountered in the initial phase of calculation, the

second-order artificial viscosity $K_2=0.25$ is used. It is noticed, however, that the calculation is unable to resume after about N=85, due to an instability conceivably caused by the stiffness. A good remedy would be to use an implicit expression to the source terms W_i instead of the present explicit form, along with more clustering in grids. Nevertheless, a global behavior is close to reality, because oxygen dissociation is completed and in a quantitatively accurate equilibrium state, while nitrogen dissociation is incomplete as pointed out in the case of using Set I.

The final phase of the analysis is performed by using Set III in Table 2 as a reaction mechanism, while the same artificial viscosity $K_2=0.25$ is used. In Set III all the elementary reactions except one are among neutral species, and therefore the chemical system is simplified including 7 species and 24 reactions. Stiffness is fairly reduced, allowing more stable calculation. A typical halfway result (N=100) is shown in Fig. 24, where the mass fraction distribution of 7 species along the stagnation streamline in the shock layer is plotted in a logarithmic scale. Since electron mass is too small, its distribution does not show up in the figure. With regard to the dissociation of molecular oxygen and nitrogen, the behavior is not essentially altered from the mechanisms in Set I or II.

7. Conclusions

A chemically reacting hypersonic flow can be handled by the Beam-Warming scheme with its explicit source terms consisting only of chemical reactions. Using 3 different mechanisms for the dissociation of oxygen and nitrogen molecules and simultaneous high-temperature reactions up to 47 in numer, the fundamental equations consisting of maximum 14 dependent variables are solved in a conventional method of inverting block-tridiagonal matrices. Although stiffness problems are coupled with temporal oscillations of physical properties inherent in the Beam-Warming scheme, it is found out that the essential difficulties can be overcome by adjusting the artificial viscosities appearing in the explicit side of the Beam-Warm-scheme. If the source terms be handled implicitly, the stiff character of the problem would have been far more improved, although instead more complicated matrices would necessitate a longer run time. However, the encountered stiffness would not have been as bad as the one in an exothermic reacting hypersonic flow like a reacting flow in a SCRAMJET (Supersonic Combustion Ramjet) engine; in an exothermic chemical process, in principle, there exist multi characteristic times.

One difficulty is a thick shock wave captured by the Beam-Warming scheme which allows chemical reaction to proceed within the otherwise infinitesimally thin width. The temperature immediately behind the shock wave is significantly lowered by this effect, conceivably changing correct characters of chemical reaction. This phenomenon, caused by the artificial viscosities that are introduced for the purpose of maintaining numerical stabilities, needs to be eliminated in the future calculations. Possible remedies are (i) grid clustering at any locations of shock wave (solution adaptive grid), (ii) a combination of shock fitting (this is also a kind of solution adaptive gridding) and the Beam-Warming scheme, and (iii) implicit source terms.

Aknowledgement

This work was supported partly by the Science Research Fund of Ministry of Education and Culture (General Research Category C No. 60550039, 1984-1986), by Drs. T. Ogawa and T. Ishiguro, the Computer Center of National Aerospace Laboratory, Tokyo, and by Profs. H. Oguchi and T. Abe, ISAS (Institute of Space and Astronautical Sciences) regarding AOTV project.

Appendix *A*

The matrices A and B defined in Eq. (32) are derived here. We define the following three quantities m, n and p:

$$\begin{aligned} m&=\rho u,\\ n&=\rho v,\\ p&=(\gamma-1)\left(e-\frac{1}{2}\rho w^2\right)\\ &=(\gamma-1)\left\{e-\frac{1}{2\rho}(m^2+n^2)\right\}, \end{aligned} \tag{90}$$

from which we obtain

$$\begin{aligned} \frac{\partial p}{\partial \rho}&=\frac{\gamma-1}{2\rho^2}(m^2+n^2),\\ \frac{\partial p}{\partial m}&=-\frac{\gamma-1}{\rho}m,\\ \frac{\partial p}{\partial n}&=-\frac{\gamma-1}{\rho}n,\\ \frac{\partial p}{\partial e}&=\gamma-1. \end{aligned} \tag{91}$$

Thus, we reach the final explicit forms:

$$A=\frac{\partial F}{\partial U}=\begin{pmatrix} 0 & 1 & 0 & 0\\ -\frac{3-\gamma}{2}u^2+\frac{\gamma-1}{2}v^2 & (3-\gamma)u & -(\gamma-1)u, & \gamma-1\\ -uv & v & u & 0\\ -\frac{\gamma eu}{\rho}+(\gamma-1)u(u^2+v^2), & \frac{\gamma e}{\rho}-\frac{\gamma-1}{2}(3u^2+v^2), & -(\gamma-1)uv, & \gamma u \end{pmatrix}, \tag{92}$$

$$B=\frac{\partial G}{\partial U}=\begin{pmatrix} 0 & 0 & 1 & 0 \\ -uv & v & u & 0 \\ \frac{3-\gamma}{2}v^2+\frac{\gamma-1}{2}u^2 & -(\gamma-1)u & (3-\gamma)v & \gamma-1 \\ -\frac{\gamma ev}{\rho}+(\gamma-1)v(u^2+v^2), & -(\gamma-1)uv, & \frac{\gamma e}{\rho}-\frac{\gamma-1}{2}(3v^2+u^2), & \gamma v \end{pmatrix}. \tag{93}$$

The matrices defined in Eq. (84) can be explicitly derived. In the process of derivation, we first calculate the following quantities:

$$\frac{\partial \rho}{\partial \rho_i}=\frac{\partial \rho_1}{\partial \rho_i}+\cdots+\frac{\partial \rho_i}{\partial \rho_i}+\cdots \qquad =1, \tag{94}$$

$$\frac{\partial(\rho_i u)}{\partial \rho_j}=u\frac{\partial \rho_i}{\partial \rho_j}+\rho_i\frac{\partial u}{\partial \rho_j}=u\frac{\partial \rho_i}{\partial \rho_j}-\rho_i\frac{u}{\rho}$$

$$=\begin{cases} -Y_i u & (i\neq j) \\ u(1-Y_i) & (i=j), \end{cases} \tag{95}$$

$$\frac{\partial(mu+p)}{\partial \rho_i}=m\frac{\partial u}{\partial \rho_i}+\frac{\partial p}{\partial \rho_i}=-\frac{mu}{\rho}+(\gamma-1)\left(\frac{m^2+n^2}{2\rho^2}-h+\frac{C_p}{R}\frac{T}{M_i}\right)$$

$$=-u^2+G(E+K_i),$$

$$G=\gamma-1,\quad E=\frac{m^2+n^2}{2\rho^2}-h,\quad K_i=\frac{C_pT}{RM_i}, \tag{96}$$

$$\frac{\partial(\rho_i u)}{\partial m}=\frac{\partial(Y_i m)}{\partial m}=Y_i+m\frac{\partial Y_i}{\partial m}=Y_i+m\left(\frac{1}{\rho}\frac{\partial \rho_i}{\partial m}-\frac{1}{\rho^2}\frac{\partial \rho}{\partial m}\right)=Y_i, \tag{97}$$

$$\frac{\partial(mu+p)}{\partial m}=u+m\frac{\partial u}{\partial m}+\frac{\partial p}{\partial m}=u+u-(\gamma-1)u=(2-G)u, \tag{98}$$

$$\frac{\partial(mu+p)}{\partial n}=\frac{\partial p}{\partial n}=-(\gamma-1)v=-Gv, \tag{99}$$

$$\frac{\partial[(e+p)u]}{\partial \rho_i}=u\frac{\partial(e+p)}{\partial \rho_i}+(e+p)\frac{\partial u}{\partial \rho_i}$$

$$=u(\gamma-1)\left(\frac{m^2+n^2}{2\rho^2}-h+\frac{C_p}{R}\frac{T}{M_i}\right)-(e+p)\frac{u}{\rho}$$

$$=uG(E+K_i)-u\left(h+\frac{m^2+n^2}{2\rho^2}-\frac{p}{\rho}+\frac{p}{\rho}\right)$$

$$=uG(E+K_i)-u\left(h+\frac{m^2+n^2}{2\rho^2}\right)$$

$$=u\left[G(E+K_i)-\left(h+\frac{m^2+n^2}{2\rho^2}\right)\right], \tag{100}$$

$$\frac{\partial[(e+p)u]}{\partial m}=(e+p)\frac{\partial u}{\partial m}+u\frac{\partial(e+p)}{\partial m}=\frac{e+p}{\rho}-u^2(\gamma-1)$$
$$=h+\frac{1}{2}(u^2+v^2)-u^2G=-E+(u^2+v^2)-u^2G, \tag{101}$$

$$\frac{\partial[(e+p)u]}{\partial n}=(e+p)\frac{\partial u}{\partial n}+u\frac{\partial(e+p)}{\partial n}=-u(\gamma-1)v=-Guv, \tag{102}$$

$$\frac{\partial[(e+p)u]}{\partial e}=(e+p)\frac{\partial u}{\partial e}+u\frac{\partial(e+p)}{\partial e}=u+u(\gamma-1)=(G+1)u, \tag{103}$$

$$\frac{\partial w_i}{\partial \rho_i}\doteqdot 0. \tag{104}$$

Thus, we reach the final forms of A, B and C:

$$A=\frac{\partial F}{\partial U}$$
$$=\begin{pmatrix} u(1-Y_1) & -uY_1 & \cdots\cdots & Y_1 & 0 & 0 \\ -uY_2 & u(1-Y_2) & \cdots\cdots & Y_2 & 0 & 0 \\ \vdots & & & \vdots & \vdots & \vdots \\ -u^2+G(E+K_1) & \cdots\cdots & & (2-G)u & -Gv & G \\ -uv & \cdots\cdots & & v & u & 0 \\ u\left[G(E+K_1)-\left(h+\frac{m^2+n^2}{2\rho^2}\right)\right] & \cdots & & -E-u^2G+(u^2+v^2), & -Guv, & (1+G)u \end{pmatrix}, \tag{105}$$

$$B=\frac{\partial G}{\partial U}$$
$$=\begin{pmatrix} v(1-Y_1) & -vY_1 & \cdots\cdots & 0 & Y_1 & 0 \\ -vY_2 & v(1-Y_2) & \cdots\cdots & 0 & Y_2 & 0 \\ \cdots & \vdots & & \vdots & \vdots & \vdots \\ -uv & & \cdots\cdots & v & u & 0 \\ -v^2+G(E+K_1) & & \cdots\cdots & -Gu & (2-G)v & G \\ v\left[G(E+K_1)-\left(h+\frac{m^2+n^2}{2\rho^2}\right)\right] & \cdots & & -Guv, & -E+(u^2+v^2)-v^2G, & (1+G)v \end{pmatrix}, \tag{106}$$

$$C=\frac{\partial W}{\partial U}=\begin{pmatrix} 0 & 0 & \cdots\cdots & 0 \\ 0 & 0 & \cdots\cdots & 0 \\ \vdots & \vdots & \ddots & \vdots \\ 0 & 0 & \cdots\cdots & 0 \\ 0 & 0 & \cdots\cdots & 0 \\ 0 & 0 & \cdots\cdots & 0 \end{pmatrix}. \tag{107}$$

Appendix *B*

The source terms of chemical reaction, the rate of mass production of each species, can be expressed for the reaction mechanism Set II as in the following:

$$\begin{aligned}\frac{d[\mathrm{N}]}{dt}=&2(k_{f,m}[\mathrm{N_2}]-k_{r,m}[\mathrm{N}]^2)[\mathrm{M}_m]+(k_{f,n}[\mathrm{NO}]-k_{r,n}[\mathrm{N}][\mathrm{O}])[\mathrm{M}_n]\\&+k_{f,34}[\mathrm{NO}][\mathrm{O}]-k_{r,34}[\mathrm{N}][\mathrm{O_2}]+k_{f,35}[\mathrm{O}][\mathrm{N_2}]-k_{r,35}[\mathrm{NO}][\mathrm{N}]\\&+k_{f,37}[\mathrm{N_2}][\mathrm{N^+}]-k_{r,37}[\mathrm{N}][\mathrm{N_2^+}]-k_{f,40}[\mathrm{N}][\mathrm{NO^+}]+k_{r,40}[\mathrm{NO}][\mathrm{N^+}]\\&-k_{f,42}[\mathrm{NO^+}][\mathrm{N}]+k_{r,42}[\mathrm{N_2^+}][\mathrm{O}]-k_{f,43}[\mathrm{O}][\mathrm{N}]+k_{r,43}[\mathrm{NO^+}][\mathrm{e^-}]\\&-2(k_{f,45}[\mathrm{N}]^2-k_{r,45}[\mathrm{N_2^+}][\mathrm{e^-}])-(k_{f,47}[\mathrm{N}]-k_{r,47}[\mathrm{N^+}][\mathrm{e^-}])[\mathrm{e^-}],\end{aligned} \tag{108}$$

$$\begin{aligned}\frac{d[\mathrm{N^+}]}{dt}=&-k_{f,37}[\mathrm{N_2}][\mathrm{N^+}]+k_{r,37}[\mathrm{N}][\mathrm{N_2^+}]+k_{f,40}[\mathrm{N}][\mathrm{NO^+}]-k_{r,40}[\mathrm{NO}][\mathrm{N^+}]\\&+(k_{f,47}[\mathrm{N}]-k_{r,47}[\mathrm{N^+}][\mathrm{e^-}])(\mathrm{e^-}],\end{aligned} \tag{109}$$

$$\begin{aligned}\frac{d[\mathrm{O}]}{dt}=&2(k_{f,l}[\mathrm{O_2}]-k_{r,l}[\mathrm{O}]^2)[\mathrm{M}_l]+(k_{f,n}[\mathrm{NO}]-k_{r,n}[\mathrm{N}][\mathrm{O}])[\mathrm{M}_n]\\&-k_{f,34}[\mathrm{NO}][\mathrm{O}]+k_{r,34}[\mathrm{N}][\mathrm{O_2}]-k_{f,35}[\mathrm{O}][\mathrm{N_2}]+k_{r,35}[\mathrm{NO}][\mathrm{N}]\\&-k_{f,38}[\mathrm{O}][\mathrm{NO^+}]+k_{r,38}[\mathrm{NO}][\mathrm{O^+}]+k_{f,39}[\mathrm{N_2}][\mathrm{O^+}]-k_{r,39}[\mathrm{O}][\mathrm{N_2^+}]\\&+k_{f,42}[\mathrm{NO^+}][\mathrm{N}]-k_{r,42}[\mathrm{N_2^+}][\mathrm{O}]-k_{f,36}[\mathrm{O}][\mathrm{O_2^+}]+k_{r,36}[\mathrm{O_2}][\mathrm{O^+}]\\&-k_{f,43}[\mathrm{O}][\mathrm{N}]+k_{r,43}[\mathrm{NO^+}][\mathrm{e^-}]-2(k_{f,44}[\mathrm{O}]^2-k_{r,44}[\mathrm{O_2^+}][\mathrm{e^-}])\\&-(k_{f,46}[\mathrm{O}]-k_{r,46}[\mathrm{O^+}][\mathrm{e^-}])[\mathrm{e^-}],\end{aligned} \tag{110}$$

$$\begin{aligned}\frac{d[\mathrm{O^+}]}{dt}=&k_{f,36}[\mathrm{O}][\mathrm{O_2^+}]-k_{r,36}[\mathrm{O_2}][\mathrm{O^+}]+k_{f,38}[\mathrm{O}][\mathrm{NO^+}]-k_{r,38}[\mathrm{O^+}][\mathrm{NO}]\\&-k_{f,39}[\mathrm{N_2}][\mathrm{O^+}]+k_{r,39}[\mathrm{O}][\mathrm{N_2^+}]+(k_{f,46}[\mathrm{O}]-k_{r,46}[\mathrm{O^+}][\mathrm{e^-}])[\mathrm{e^-}],\end{aligned} \tag{111}$$

$$\frac{d[N_2^+]}{dt}=k_{f,37}[N_2][N^+]-k_{r,37}[N][N_2^+]+k_{f,39}[N_2][O^+]-k_{r,39}[O][N_2^+]$$
$$+k_{f,42}[NO^+][N]-k_{r,42}[N^+][NO]+k_{f,45}[N]^2-k_{r,45}[N_2^+][e^-], \tag{112}$$

$$\frac{d[N_2]}{dt}=(-k_{f,m}[N_2]+k_{r,m}[N]^2)[M_m]-k_{f,35}[O][N_2]+k_{r,35}[NO][N]$$
$$-h_{f,37}[N_2][N^+]+k_{r,37}[N][N_2^+]-k_{f,39}[N_2][O^+]+k_{,39}[O][N_2^+], \tag{113}$$

$$\frac{d[NO]}{dt}=(-k_{f,n}[NO]+k_{r,m}[N][O])[M_n]-k_{f,34}[NO][O]+k_{r,34}[N][O_2]$$
$$+k_{f,35}[O][N_2]-k_{r,35}[NO][N]+k_{f,38}[O][NO^+]-k_{r,38}[O^+][NO]$$
$$+k_{f,40}[N][NO^+]-k_{r,40}[NO][N^+]+k_{f,41}[O_2][NO^+]$$
$$-k_{r,41}[NO][O_2^+], \tag{114}$$

$$\frac{d[O_2]}{dt}=(-k_{f,l}[O_2]+k_{r,l}[O]^2)[M_l]+k_{f,34}[NO][O]-k_{r,34}[O_2][N]$$
$$+k_{f,36}[O][O_2^+]-k_{r,36}[O^+][O_2]-k_{f,41}[O_2][NO^+]$$
$$+k_{r,41}[NO][O_2^+], \tag{115}$$

$$\frac{d[NO^+]}{dt}=-k_{f,38}[O][NO^+]+k_{r,38}[NO][O^+]-k_{f,40}[N][NO^+]$$
$$+k_{r,40}[NO][N^+]-k_{f,41}[O_2][NO^+]+k_{r,41}[NO][O_2^+]$$
$$-k_{f,42}[NO^+][N]+k_{r,42}[N_2^+][O]+k_{f,43}[O][N]-k_{r,43}[NO^+][e^-], \tag{116}$$

$$\frac{d[O_2^+]}{dt}=-k_{f,36}[O][O_2^+]+k_{r,36}[O_2][O^+]+k_{f,41}[O_2][NO^+]$$
$$-k_{r,41}[O_2^+][NO]+k_{f,44}[O]^2-k_{r,44}[O_2^+][e^-], \tag{117}$$

$$\frac{d[e^-]}{dt}=k_{f,43}[O][N]-k_{r,43}[NO^+][e^-]+k_{f,44}[O]^2-k_{r,44}[O_2^+][e^-]$$
$$+k_{f,45}[N]^2-k_{r,45}[N_2^+][e^-]+(k_{f,46}[O]-k_{r,46}[O^+][e^-])[e^-]$$
$$+(k_{f,47}[N]-k_{r,47}[N^+][e^-])[e^-],$$
where $l=1\sim11,\ m=12\sim22,\ n=23\sim33.$ (118)

References

1) H. C. Yee and J. L. Shinn; Semi-Implicit and Fully Implicit Shock Capturing Methods for Hyperbolic Conservation Laws with Stiff Source Terms, AIAA Paper 87-1116, Honolulu, 1987.
2) J. P. Boris and D. Book; Meth. in Comp. Phys. Vol. 16, Chapter II, Academic Press, 1976.
3) S. Taki and T. Fujiwara; Numerical Simulation of Triple Shock Behavior of Gaseous Detonation, 18th International Symposium on Combustion, pp. 1671-1681, 1981.
4) T. A. Zang, J. P. Drummond, G. Erlebacher, C. Speziale and M. Y. Hussaini; Numerical Simulation of Transition, Compressible Turbulence, and Reacting Flows, AIAA Paper 87-0130, Reno, 1987.
5) D. Desautel; Shock Tunnel Measurements of AOTV Bow Shock Location, Proceedings of 15th International Symposium on Shock Waves and Shock Tubes, Stanford University Press, pp. 803-809, 1986.
6) C. Park; A Review of Shock Waves around Aeroassisted Orbital Transfer Vehicles, ibid., pp. 27-41, 1986.
7) Yi-Yun Wang and T. Fujiwara; Numerical Analysis of Transonic Flow around a Two-Dimensional Airfoil by Solving Full Navier-Stokes Equations, Memoirs of the Faculty of Engineering, Nagoya Univ. Vol. 36, No. 2, pp. 138-178, November 1984.
8) T. H. Pulliam and J. L. Steger; Recent Improvements in Efficiency, Accuracy and Convergence for Implicit Approximate Factorization Algorithms, AIAA Paper 85-0360.
9) W. D. Hayes and R. F. Probstein; Hypersonic Flow Theory Vol. 1, Inviscid Flows, Academic Press, 1966.
10) A. H. Shapiro; The Dynamics and Thermodynamics of Compressible Fluid Flow Vol. 1, The Ronald Press Company, 1953.
11) C. Park; On Convergence of Computation of Chemically Reacting Flows, AIAA Paper 85-0247.
12) H. W. Liepmann and A. Roshko; Elements of Gasdynamics, John Wiley and Sons, 1957.
13) K. Masuda; Thermogasdynamics of AOTV, Master Thesis, Department of Aeronautical Engineering, Nagoya University, 1985.
14) T. Fujiwara and K. Horie; Real Gas Flow and Heat Transfer to a Hypersonic Vehicle, 18th Fluid Dynamics Symposium of Japan, pp. 10-13, 1985.
15) S. Ohbayashi, K. Fujii and K. Kuwahara; LU-ADI Method and Boundary Condition for Navier-Stokes Equations, 17th Fluid Dynamics Symposium of Japan, pp. 30-33, 1985.
16) Y. Ohmori and T. Fujiwara; Numerical Fluid Dynamics Analysis for a Three-Dimensional Supersonic Vehicle, 23th Central and Western Section Autumn Conference of JSASS, pp. 113-116, 1986.
17) J. Kondo; Highspeed Aerodynamics, Corona Company, 1977.

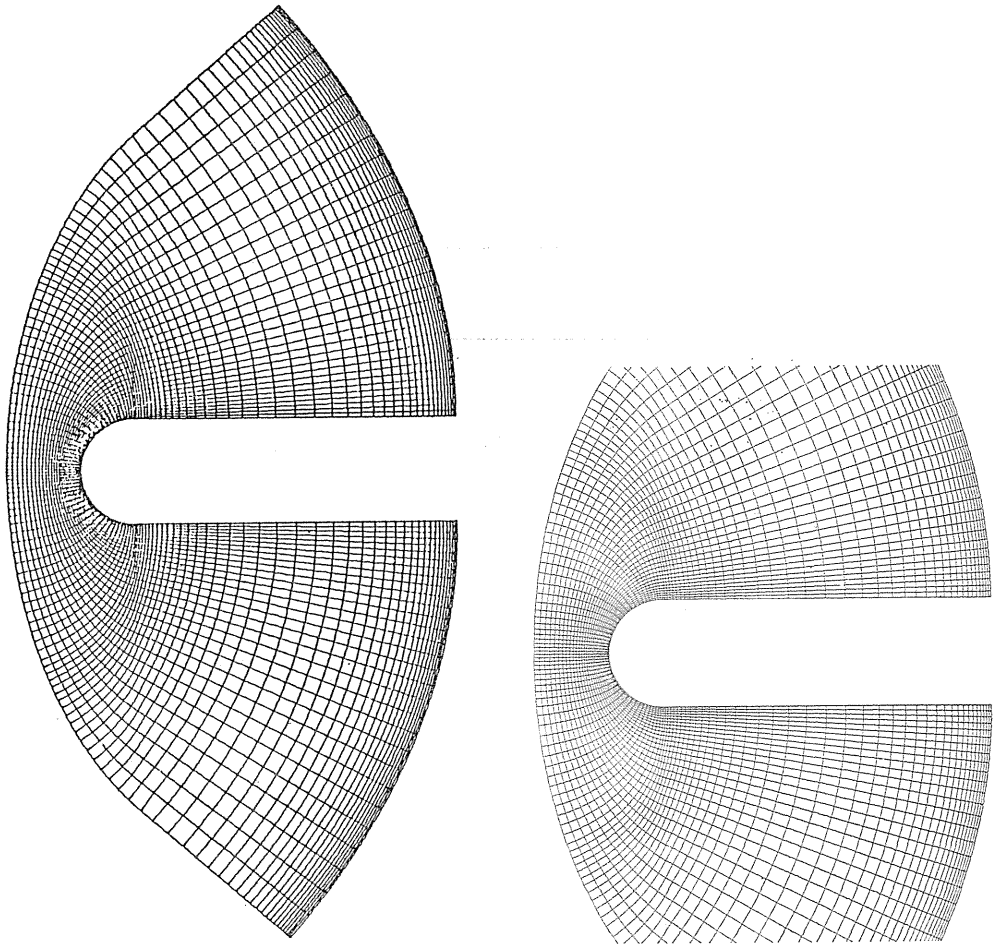

(a) (b)

Fig. 1. (a) The algebraic grid utilized to solve an ideal flow at $M_\infty=25.2$ where there is no chemical reaction.
(b) A detailed distribution of grid points (total 129×31).

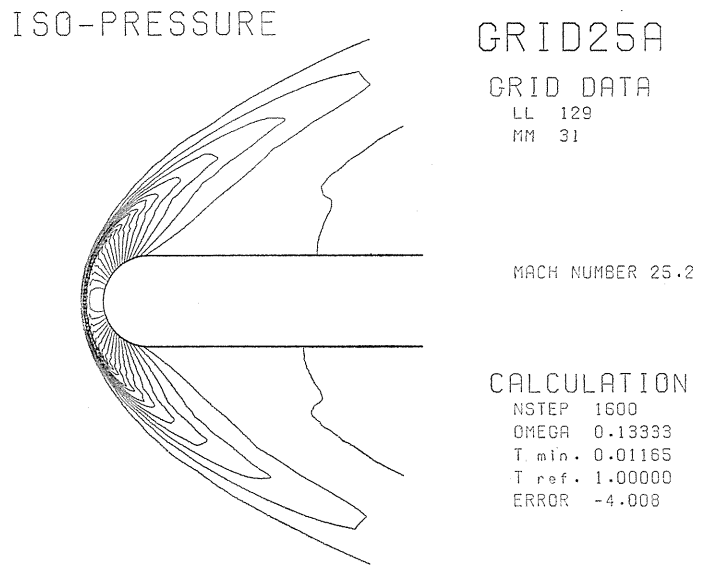

Fig. 2. The pressure distribution in an ideal hypersonic flow of $M_\infty=25.2$ around a blunt body at angle of attack zero. Convergence criterion is that the sum of the residues of all the dependent variables, per grid point, decreases below 10^{-6}, which is realized at N=1600 steps.

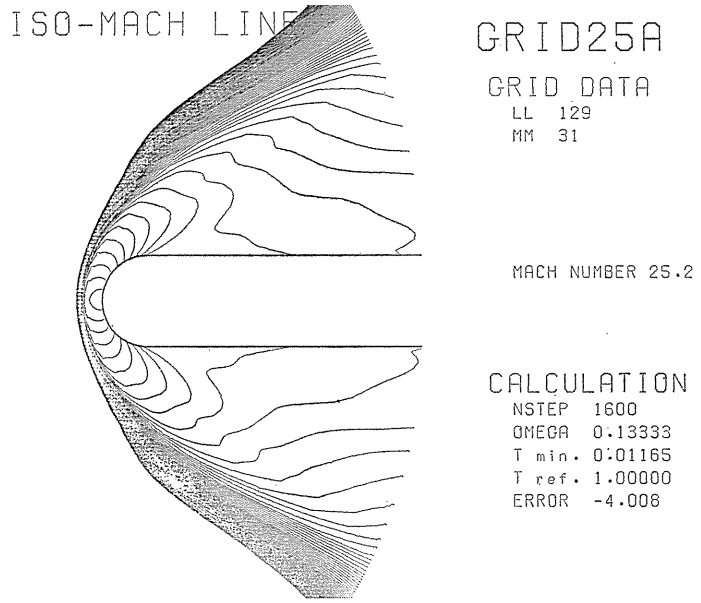

Fig. 3. The Mach number distribution in an ideal hypersonic flow at $M_\infty=25.2$.

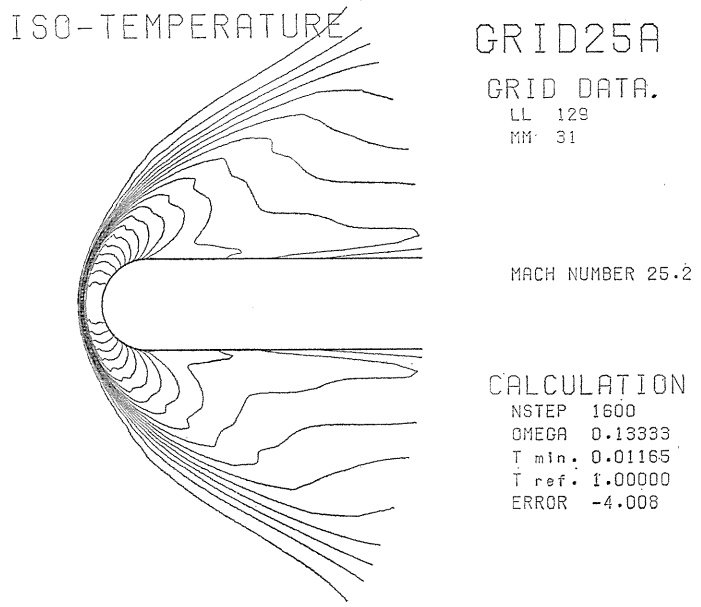

Fig. 4. Iso-temperature lines in an ideal hypersonic flow at $M_\infty=25.2$.

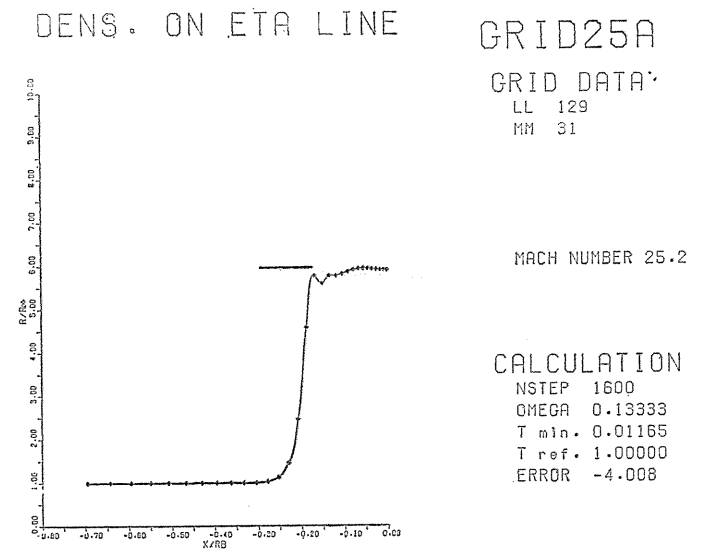

Fig. 5. The density distribution along the stagnation streamline in the shock layer in front of a blunt body at angle of attack zero and $M_\infty=25.2$, where no chemical reactions are taken into consideration and the gas is assumed ideal. The Rankine-Hugoniot relation (a horizontal solid line) is held correctly, while a Gibbs phenomenon is observed immediately behind the shock wave, due to a low artificial viscosity.

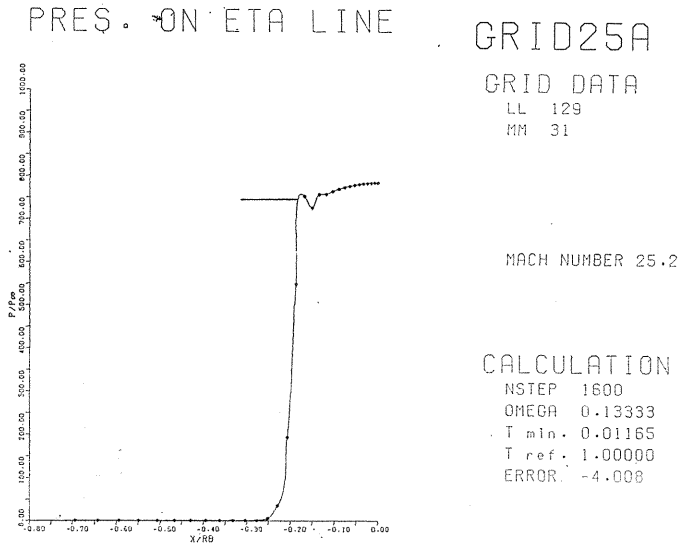

Fig. 6. The pressure distribution along the stagnation streamline in the shock layer of an ideal gas, showing a good agreement with the Rankine-Hugoniot relation (a horizontal solid line) with $\gamma=1.4$.

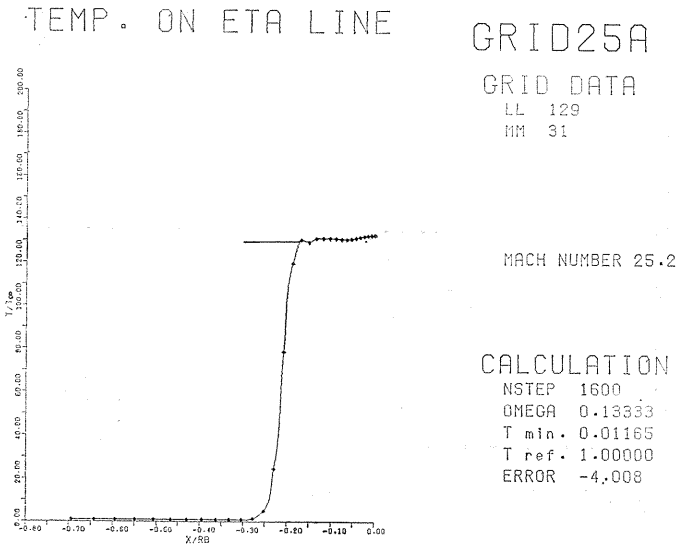

Fig. 7. The temperature distribution along the stagnation streamline in the shock layer of an ideal gas.

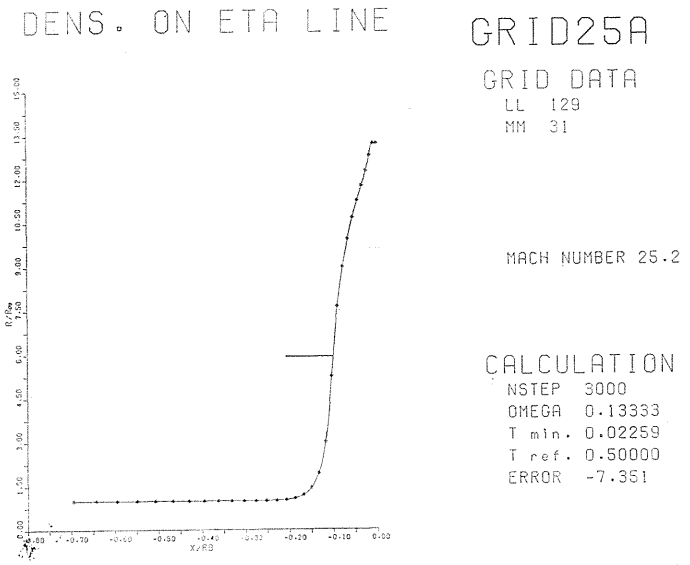

Fig. 8. The density distribution along the stagnation streamline in the shock layer at $M_\infty=25.2$, where the chemical reaction Set I shown in Table 1 is utilized. It is noticed that the density greatly increases while the shock standoff distance is remarkably reduced by the dissociation of oxygen and nitrogen molecules. At time step N=3000 the residual decreased down to $10^{-7.35}$, showing a rapid convergence, conceivably due to a large artificial viscosity $K_2=0.30$ compared with the other cases.

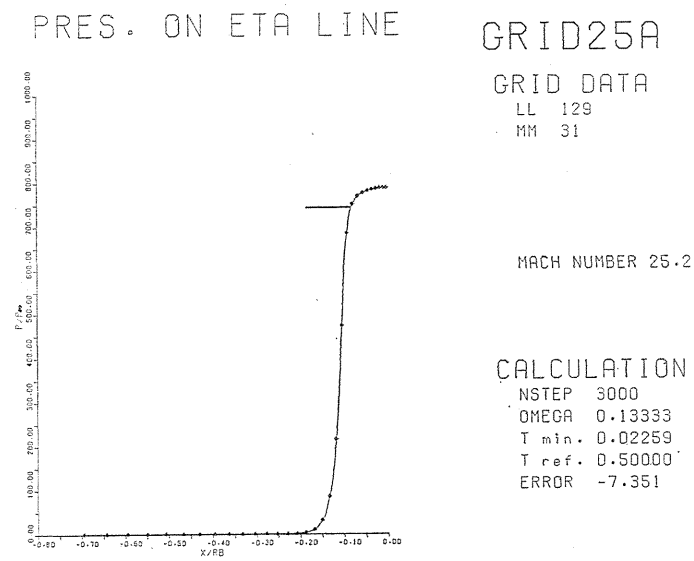

Fig. 9. The pressure distribution along the stagnation streamline in the shock layer for the chemical reactions in Set I. Considerable deviation from the Rankine-Hugoniot relation (a horizontal solid line) is caused by a thick bow shock wave as a resulti of the Beam-Warming technique; chemical reacton can proceed within the otherwise infinitesimally thin inert shock wave.

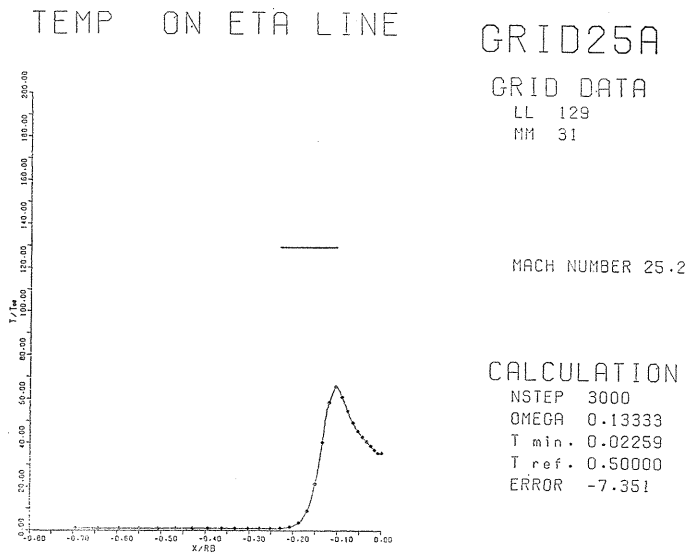

Fig. 10. The temperature distribution along the stagnation streamline in the shock layer for the chemical reactions in Set I. Because of the dissociating endothermic chemical reaction within the thick bow shock wave inherent in the Beam-Warming scheme, the temperature is greatly reduced from the Rankine-Hugoniot relation. The shock wave becomes thicker due to a high second-order artificial viscosity $K_2=0.30$.

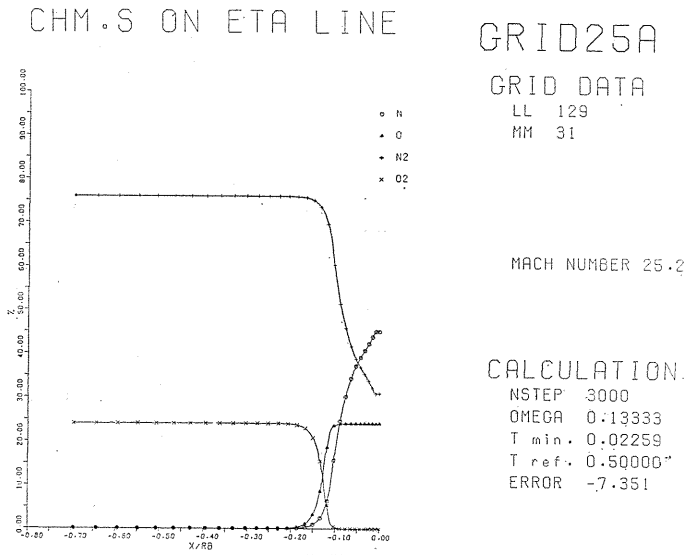

Fig. 11. The concentration distribution of each chemical species along the stagnation streamline for the chemical reactions in Set I. Oxygen dissociation has reached equilibrium in the shock layer while nitrogen is still chemically non-equilibrium. Measuring from the body surface 0.00, the shock standoff distance non-dimensionalized by the radius of the blunt body is 0.16, in good agreement with existing experimental or calculated results.

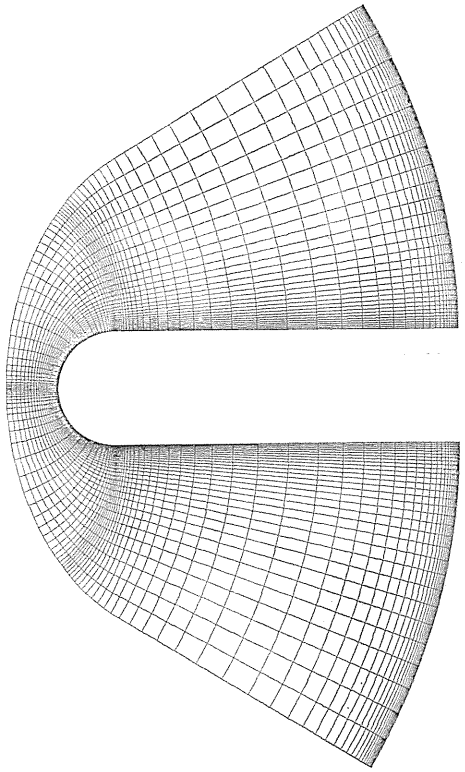

Fig. 12. A grid system utilized for chemically reacting flows where the chemical reactions in Set I or in Set II are considered. Although the grid number is held identical with the case in Fig. 1 (31×129), the clustering is clearly seen different.

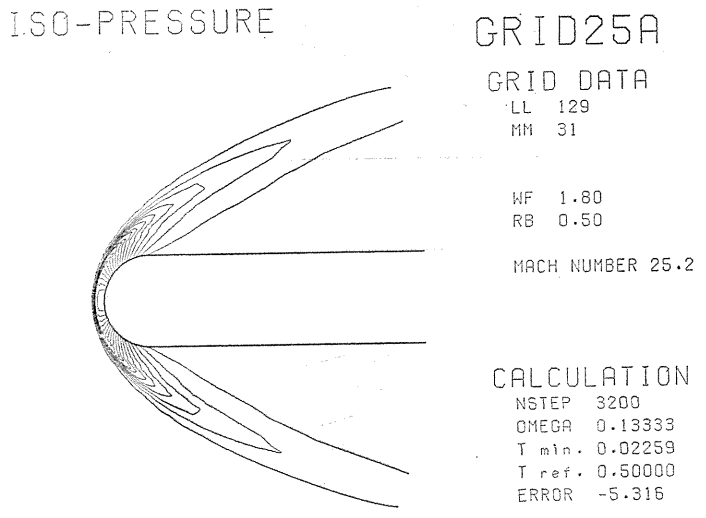

Fig. 13. Overall pressure distribution for a chemically reacting flow using Set I around a blunt body with angle of attack zero at $M_\infty=25.2$. Convergence criterion $10^{-5.316}$ is realized at N=3200 steps. In contrast with the case shown in Figs. 8~11, a smaller artificial viscosity $K_2=0.15$ is used to yield, in principle, a thinner bow shock and an increased Gibbs phenomenon.

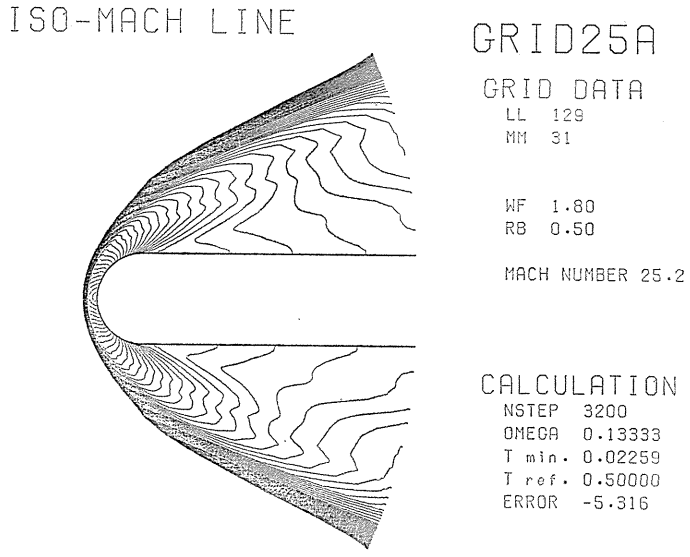

Fig. 14. Mach number distribution for a chemically reacting flow using Set I and $K_2=0.15$.

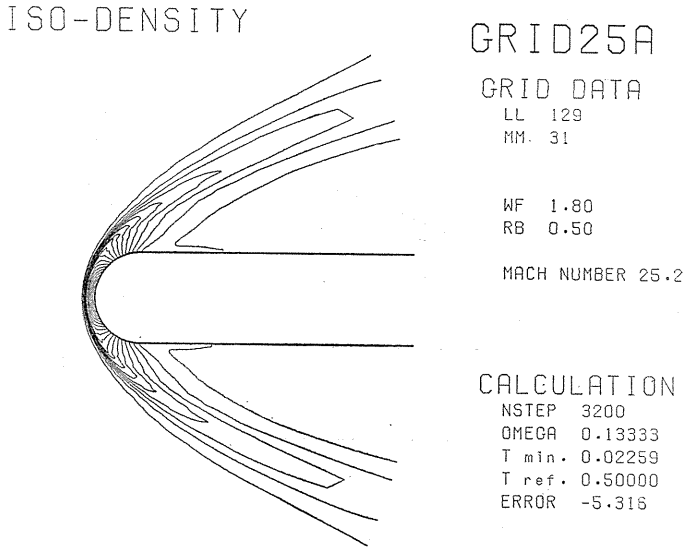

Fig. 15. Density distribution for a chemically reacting flow using Set I and $K_2=0.15$.

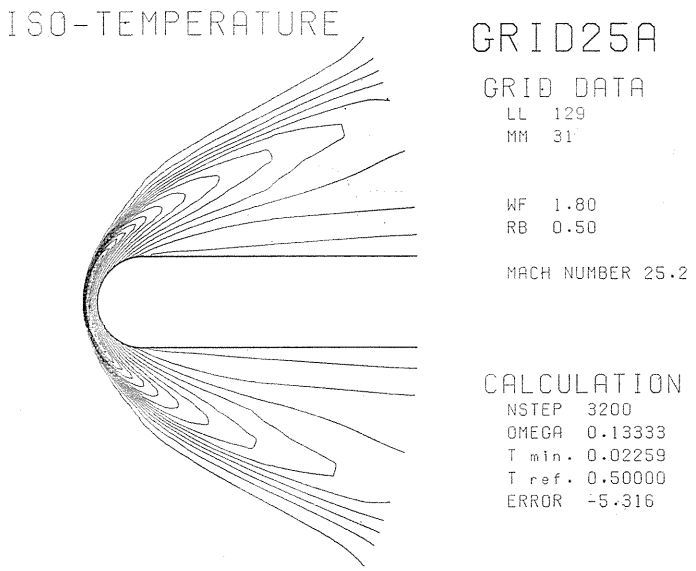

Fig. 16. Temperature distribution for a chemically reacting flow using Set I and $K_2=0.15$.

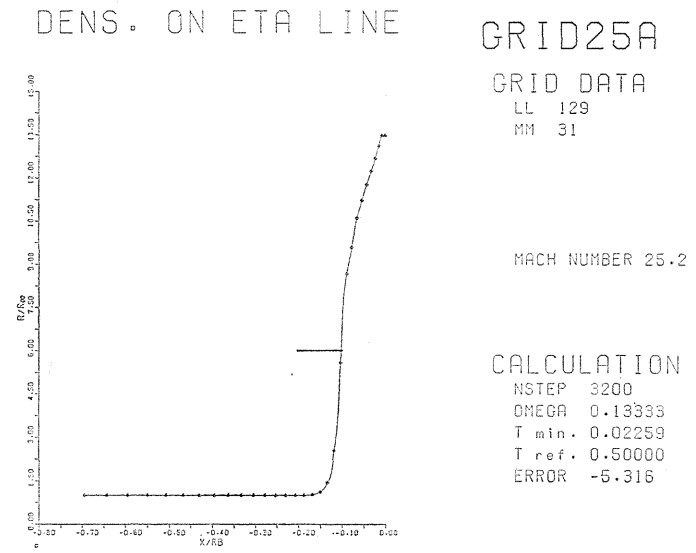

Fig. 17. The density distribution along the stagnation streamline for a chemically reacting flow using Set I and $K_2=0.15$. The deviation from the Rankine-Hugoniot relation is large due to the chemical reaction within a bow shock wave. However, because of a thinner shock wave caused by a lower artificial viscosity $K_2=0.15$, the value immediately behind the shock is seen slightly closer to the Rankine-Hugoniot relation (compared with Fig. 8).

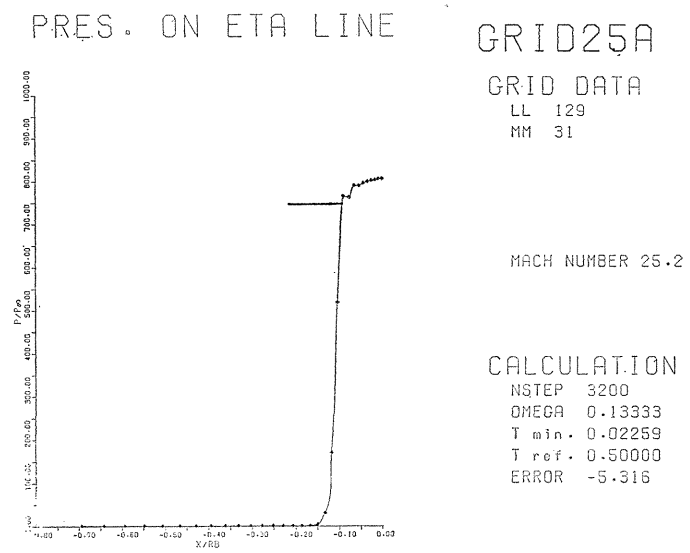

Fig. 18. The pressure distribution along the stagnation streamline for a chemically reacting flow using Set I and $K_2=0.15$. Due to the lower artificial viscosity a considerable Gibbs phenomenon is seen immediately behind a bow shock wave. The deviation from the Rankine-Hugoniot relation is much smaller compared with the density in Fig. 17 and the temperature in Fig. 19.

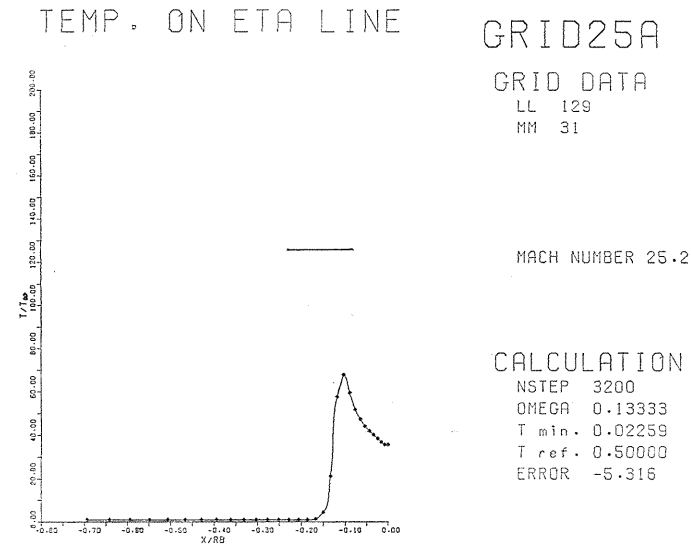

Fig. 19. The temperature distribution along the stagnation streamline for a chemically reacting flow using Set I and $K_2=0.15$. Compared with Fig. 10, the deviation from the Rankine-Hugoniot relation is mitigated due to the obvious sharpness of a bow shock wave.

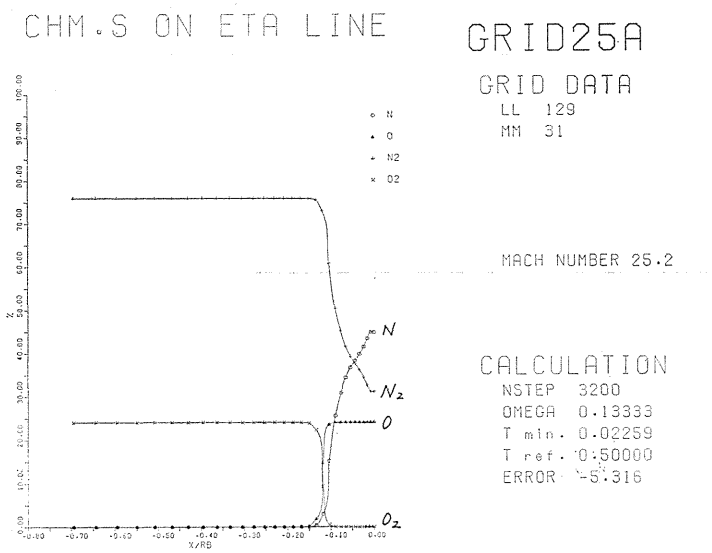

Fig. 20. The distribution of chemical species along the stagnation streamline for a chemically reacting flow using Set I and $K_2=0.15$. Except for the thickness of a bow shock wave, there is no significant difference from Fig. 11.

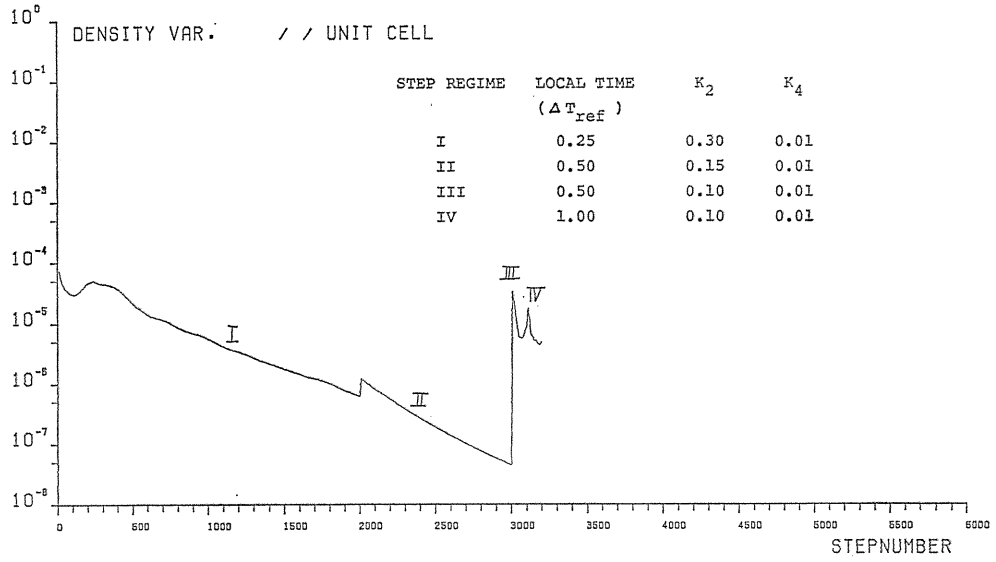

Fig. 21. The temporal behavior of the residue of the continuity equation during the solution process of a case (chemical reaction Set I and $K_2=0.15$). Both the local time and the second-order artificial viscosity were changed during a case for the purpose of reducing the thickness of a bow shock. As seen in the behavior, a sudden rise of error is caused by the reduction of artificial viscosity and by the increase of time step, in particular, at Regime Ⅲ.

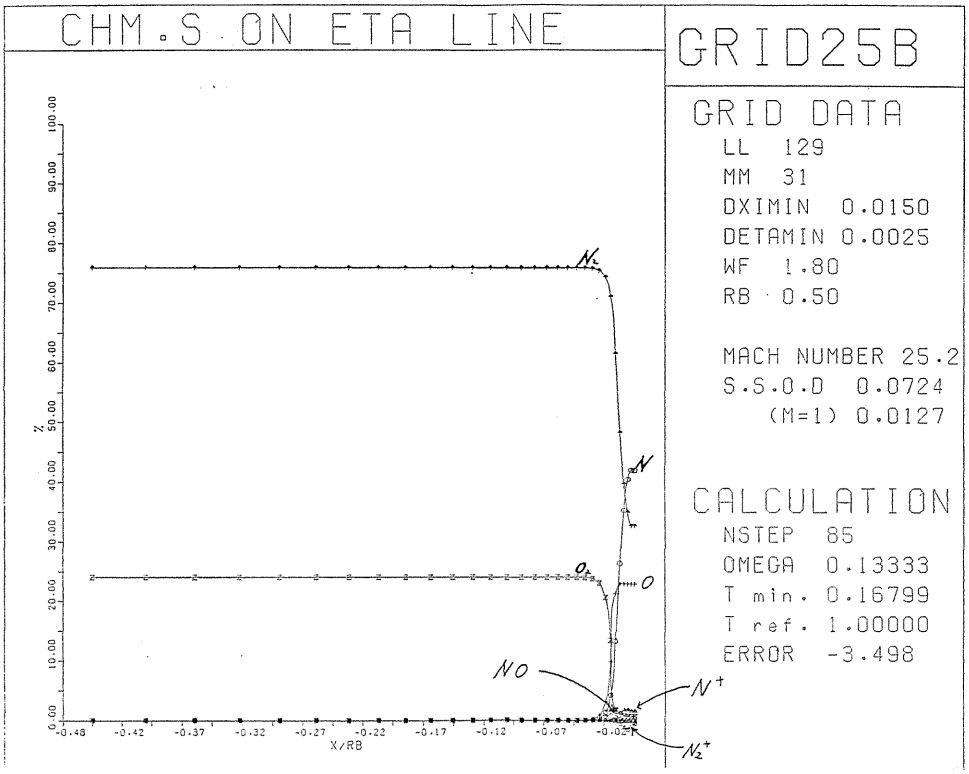

Fig. 22. The distribution of chemical species along the stagnation streamline for a reacting flow using Set II (47 elementary reactions) and $K_2=0.25$. The results at N=85 steps yet to converge. Serious stiffness is encountered.

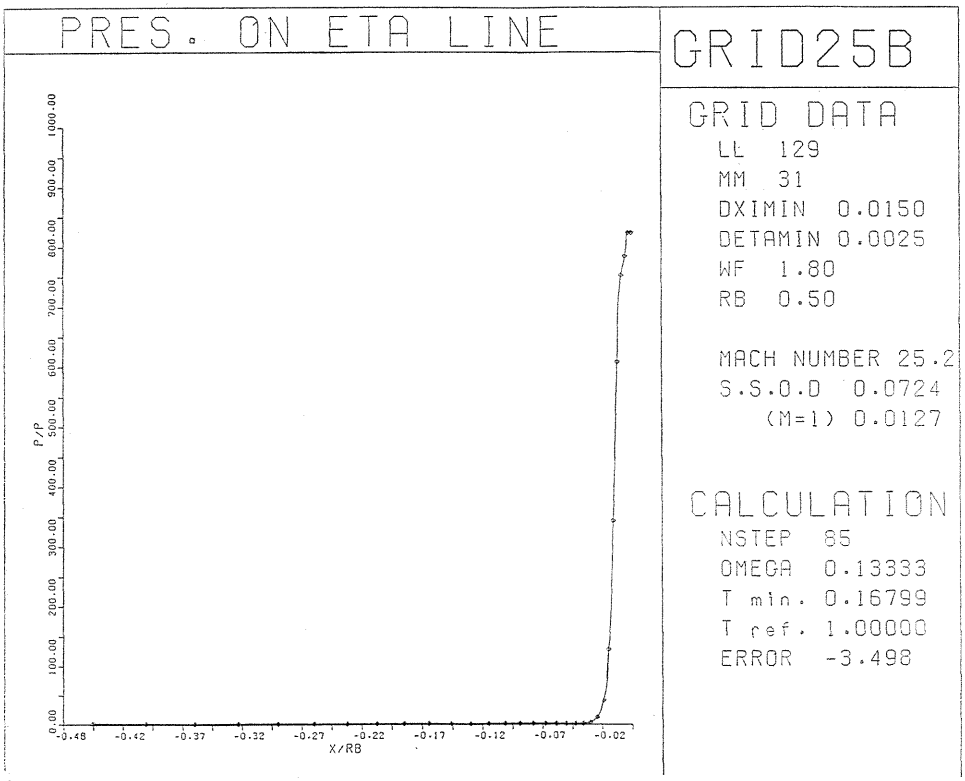

Fig. 23. The pressure distribution along the stagnation streamline for a chemically reacting flow using Set Ⅱ and $K_2=0.25$, at N=85.

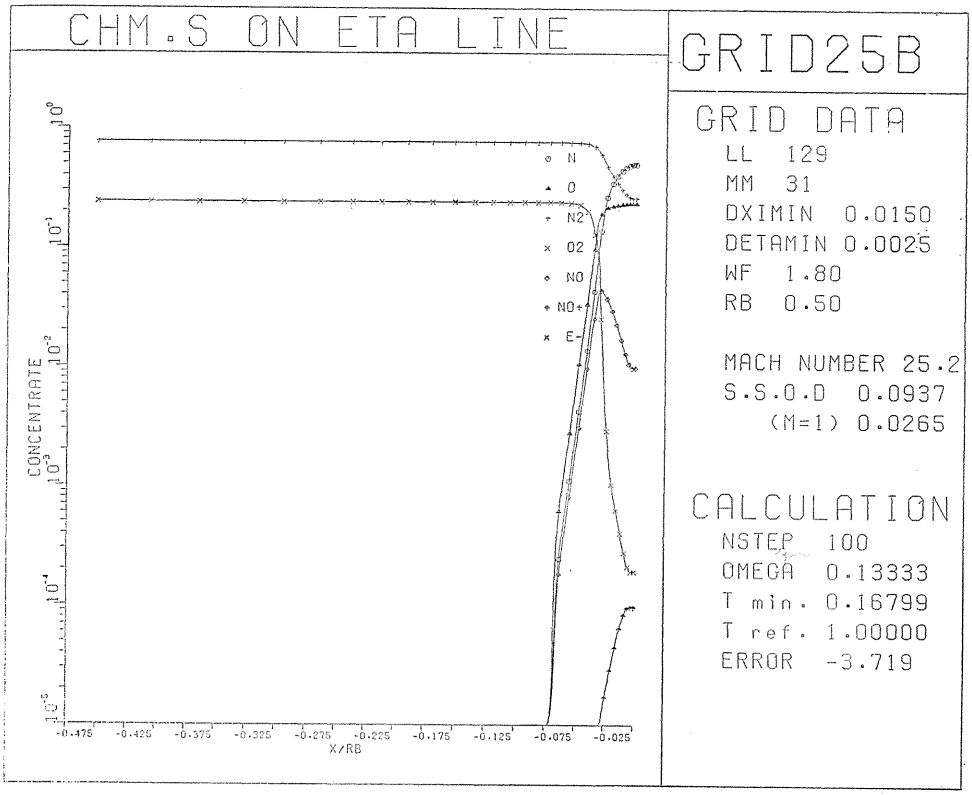

Fig. 24. The concentration distribution of chemical species along the stagnation streamline for a chemically reacting flow using Set Ⅱ (only the reactions with superscript * in Table 2) and $K_2=0.25$. The results are at N=100 yet to converge. Stiffness problem is mitigated due to the elimination of a number of ion participating elementary reactions.

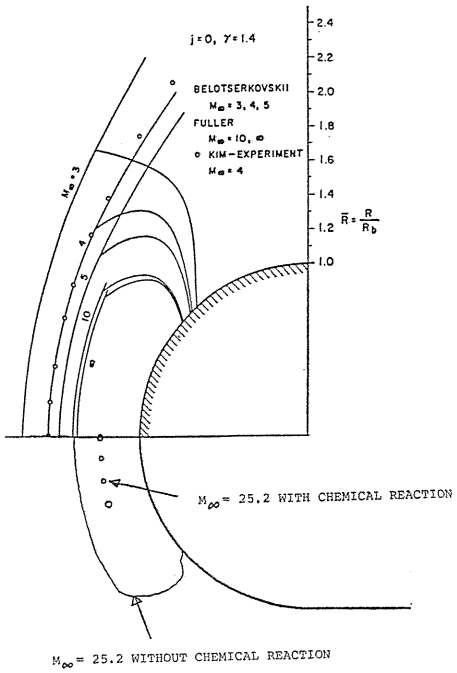

Fig. 25. The shock standoff distance calculated with/without chemical reactions (Set I and $K_2=0.15$) is compared with the existing experiments and theories. The present ideal gas results of $M_\infty=25.2$ are successfully located between $M_\infty=10$ and ∞ of the theoretical results. The inclusion of endothermic chemical reactions drastically reduces the shock standoff distance, as indicated by the open circles.

Memoirs of the Faculty of Engineering, Nagoya University
vol. 39, No. 2 (1987)

Part II.

A HYBRID TECHNIQUE FOR HYPERVELOCITY FLOWS AROUND A RE-ENTRY VEHICLE WITH REAL GAS EFFECTS

K. V. REDDY and TOSHI FUJIWARA

Abstract

A computational procedure which is capable of determining the three-dimensional flowfield surrounding a reentry body traveling at hypersonic velocity in a real gas medium is presented. The strong peripheral shock treated as sharp discontinuity is automatically generated as part of the solution. The governing equations in conservational law form are solved using an implicit finite-difference scheme between the peripheral shock and the body, using a floating mesh system. Resulting two-dimensional as well as three-dimensional flowfields about a typical blunt-nosed reentry body are illustrated for various hypersonic Mach numbers. The differences between perfect gas and real gas are discussed.

1. Introduction

The flowfields around a vehicle re-entering into atmosphere are characterized by a peripheral bow shock, multiple internal shocks, expansion waves and slip surfaces. Because of the size of the vehicle and the low temperature and high velocity freestream requirements, the flow cannot be easily simulated by current ground based facilities. Hence numerical computation of such flowfields is of considerable interest to the vehicle designer. There are at least two numerical approaches for calculating flows with discontinuities in flow variables. In one, flow discontinuities are treated separately and independently by applying appropriate Rankine-Hugoniot relations or slip surface conditions. Although it is conceptually possible to treat all the shock waves and slip surfaces as sharp discontinuities, the method would involve complex logics and would be particularly difficult to setup for automatic computation. The other procedure which uses shock capturing

techniques is inherently capable of predicting the location and strength of all the shocks without explicit use of any shock fitting procedures. However, the shocks captured by these methods spread over several mesh intervals and require a sufficient number of grid points to accurately capture them. The well known numerical algorithms such as MacCormack's second-order non-centered difference algorithm, Beam-Warming's implicIt one and Harten's TVD schemes are proved to be capable of capturing these shocks in ideal gas flows very accurately. When the temperature in the flow regime is high enough to cause the flow to dissociate, then the ideal gas formulation of the problem is no longer valid and one has to consider the real gas effects and chemical reactions that occur in the flow regime. The diffused captured shock and the oscillation in the temperature associated with the captured shock may change the chemical composition of the flow medium in the neighborhood of the shock wave, and the capability of these algorithms to capture the shock in a reacting flow is yet to be proved.

Fortunately, as the strongest shock associated with a reentry vehicle turns out to be the peripheral shock, it seems plausible that in order to improve efficiency and accuracy of the numerical algorithm and at the same time to alleviate the problems encountered in locating and treating all shocks as sharp discontinuities, a hybrid scheme that treats the peripheral shock as sharp shock and captures all the other shocks may be appropriate. Similar hybrid schemes are developed by Thomas et al. (1) for ideal gases and Kutler et al. (2) for real gases. They all constructed explicit hybrid schemes. In the last decade, since the introduction of an efficient implicit shock capturing scheme by Beam and Warming (3), a number of authors have calculated various flowfields over a variety of geometries where the scheme has been proved successful in calculating ideal flows. In particular, implicit schemes are superior to explicit ones in handling stiffness problems associated with nonequilibrium flows. The purpose of the present work is to construct a hybrid implicit scheme to solve flowfields over a rocket nose configuration moving at hypersonic velocities in a real gas medium.

2. Governing Equations

The fluid dynamic equations in conservation-law form for an unsteady, inviscid, three-dimensional and compressible flow can be written in ξ, η, ζ, τ general coordinates (4) as follows:

$$\partial_\tau \hat{q}+\partial_\xi \hat{E}+\partial_\eta \hat{F}+\partial_\zeta \hat{G}=0, \tag{1}$$

where

$$\hat{q}=J^{-1}\begin{pmatrix} \rho \\ \rho u \\ \rho v \\ \rho w \\ e \end{pmatrix}, \qquad \hat{E}=J^{-1}\begin{pmatrix} \rho U \\ \rho uU+\xi_x p \\ \rho vU+\xi_y p \\ \rho wU+\xi_z p \\ (e+p)U-\xi_t p \end{pmatrix},$$

$$\hat{F}=J^{-1}\begin{pmatrix}\rho V\\ \rho uV+\eta_x p\\ \rho vV+\eta_y p\\ \rho wV+\eta_z p\\ (e+p)V-\eta_t p\end{pmatrix},\qquad \hat{G}=J^{-1}\begin{pmatrix}\rho W\\ \rho uW+\zeta_x p\\ \rho vW+\zeta_y p\\ \rho wW+\zeta_z p\\ (e+p)W-\zeta_t p\end{pmatrix},$$

and

$$U=\xi_t+\xi_x u+\xi_y v+\xi_z w,$$

$$V=\eta_t+\eta_x u+\eta_y v+\eta_z w,$$

$$W=\zeta_t+\zeta_x u+\zeta_y v+\zeta_z w.$$

In this formulation, the cartesian velocity components u, v and w are retained as independent variables and the velocity components U, V and W are contravariant velocities written without metric normalization. Here the velocities are nondimensionalized with respect to a_∞ (the freestream speed of sound), the density ρ is referenced to ρ_∞ and the total energy e and pressure p are nondimensionalized with respect to $\rho_\infty a_\infty^2$. The pressure p is given by the equation

$$p=h+0.5\times\rho(u^2+v^2+w^2)-e, \tag{2}$$

where the enthalpy is nondimensionalized by a_∞^2.

The temperature T is obtained from the equation of state

$$T=p/\rho\overline{R}, \tag{3}$$

where $\overline{R}$ is the gas constant equal to R_0/M, with R_0 as the universal gas constant (8.3144 J/gm·mole·K) and M as the molecular weight of the gas. In the present formulation the gas medium is considered to be air with 79 percent nitrogen and 21 percent oxygen.

The enthalpy h is a thermodynamic property, a function of temperature only. In the case of an ideal gas h can be related to ρ and p as $h=\gamma/(\gamma-1)p/\rho$; but in the case of a real gas no such simple explicit functional relationships exist. The usual procedure in evaluating a real gas state relation is to use a combination of table lookup and curve fitting procedures. In the present work, thermodynamic properties h and c (specific heat) are generated for air from the data obtained for nitrogen and oxygen using JANAF Tables (5) at various temperatures. For a given temperature state properties are calculated by interpolating the data at two neighboring temperatures using spline curves.

Metric terms appearing in the governing equations are obtained from chain-rule expansion of x_ξ, y_ξ, etc. and are solved for ξ_x, ξ_y, etc. to give

$$\xi_x=J(y_\eta z_\zeta-y_\zeta z_\eta),\qquad \eta_x=J(y_\zeta z_\xi-y_\xi z_\zeta),$$

$$\xi_y=J(z_\eta x_\zeta-z_\zeta x_\eta),\qquad \eta_y=J(z_\zeta x_\xi-z_\xi x_\zeta),$$

$$\xi_z=J(x_\eta y_\zeta-x_\zeta y_\eta),\qquad \xi_t=-x_\tau\xi_x-y_\tau\xi_y-z_\tau\xi_z,$$

$$\zeta_x = J(y_\xi z_\eta - y_\eta x_\zeta), \qquad \eta_t = -x_\tau \eta_x - y_\tau \eta_y - z_\tau \eta_z,$$

$$\zeta_y = J(z_\xi x_\eta - z_\eta x_\xi), \qquad \zeta_t = -x_\tau \zeta_x - y_\tau \zeta_y - z_\tau \zeta_z,$$

$$\zeta_z = J(x_\xi y_\eta - x_\eta y_\xi),$$

and

$$J^{-1} = x_\xi y_\eta z_\zeta + x_\zeta y_\xi z_\eta + x_\eta y_\zeta z_\xi - x_\xi y_\zeta z_\eta - x_\eta y_\xi z_\zeta - x_\zeta y_\eta z_\xi.$$

3. Grid System

Nose portion of a reentering rocket is shown in Fig. 1. The simplified body geometry consists of a sphere-cone portion and a long cylindrical portion. A body-oriented coordinate system shown in Fig. 1 is chosen in order to simplify the boundary treatment. The grid system consists of fixed radial rays (ξ=const and ζ=const) and floating η=const surfaces. The innermost η=const surface coincides with the body surface and the outermost one always coincides with the moving shock surface. All the other η=const grid surfaces filling the shock layer are distributed exponentially between these two boundary surfaces. Exponential stretching is used to allow grid points to concentrate near the body surface and the peripheral shock surface; and the transformation equations are given by

$$\left.\begin{aligned} \eta &= a_1(e^{\beta_1 \eta^*} - 1.0) \quad \text{for } 0 \leq \eta^* \leq \eta_c^*, \\ \eta &= 1 + a_2[1.0 - e^{\beta_2(1-\eta^*)}] \quad \text{for } \eta_c^* \leq \eta^* \leq 1, \end{aligned}\right\} \tag{4}$$

where a_1, a_2, β_1 and β_2 are the constants to be determined from the given grid spacings near the body and near the shock wave and the value of η_c^* is usually set equal to 0.5 (η_c^* represents the point at which both of the algebraic expressions should give the same value). Clustering grid points near the shock wave is necessary to decay the propagation of oscillations in the flow variables generated at the shock wave. Though, for real gas inviscid flow calculations, clustering of grid points near the body is generally not necessary, it is required especially when the method is extended to calculate reacting and viscous flows.

4. Numerical Method

A finite-difference form of the governing equations has to be integrated between the shock and body surfaces from the given initial conditions to yield a time-evolving solution. Since we are interested only in a steady solution, the integration in t direction should be carried out until the solution converges to a steady one. Once the solution becomes steady, it is assumed that the peripheral shock has moved to its equilibrium position and the mesh velocities at all grid points have become zero.

The governing equations given by Eq. (1) are approximated by adopting the noniterative approximate factorization implicit method of Beam and Warming as follows:

$$[I+\Delta\tau\delta_\xi\hat{A}^n-\Delta\tau D_i|_\xi][I+\Delta\tau\delta_\eta\hat{B}^n-\Delta\tau D_i|_\eta]$$
$$[I+\Delta\tau\delta_\zeta\hat{C}^n-\Delta\tau D_i|_\zeta]\Delta\hat{q}^n=-\Delta\tau(\delta_\xi\hat{E}^n+\delta_\eta\hat{F}^n+\delta_\zeta\hat{G}^n+D_e\hat{q}^n), \tag{5}$$

where $\hat{A}$, $\hat{B}$ and $\hat{C}$ are the Jacobian matrices $\frac{\partial\hat{E}}{\partial\hat{q}}$, $\frac{\partial\hat{F}}{\partial\hat{q}}$, and $\frac{\partial\hat{G}}{\partial\hat{q}}$. The Jacobian matrices are given in Appendix. Here δ_ξ, δ_η and δ_ζ are typical three point central difference approximations that are second-order accurate, so that the factored left-hand-side operator forms block tridiagonal matrics. The operators ∇ and Δ simple backward and forward differences. The terms D_i denote the numerical dissipative terms given by

$$D_i|_\xi=\epsilon_i J^{-1}(\nabla\Delta)_\xi J,\ D_i|_\eta=\epsilon_i J^{-1}(\nabla\Delta)_\eta J,\ D_i|_\zeta=\epsilon_i J^{-1}(\nabla\Delta)_\zeta J. \tag{6}$$

The operators D_i which are inserted into the respective implicit block operators are central three point second-order differences. The dissipative term D_e added to the explicit side of the algorithm is a combination of second-order and fourth-order smoothing terms (6). Second-order smoothing terms added in order to dissipate the severe oscillations that occur near the internal shocks are effective only when there are large gradients in density values. The numerical dissipation model used for D_e is of the form

$$D_e=\nabla_\xi(\sigma_{j+1,k}J^{-1}_{j+1,k}+\sigma_{j,k}J^{-1}_{j,k})(\epsilon^{(2)}_{j,k}\Delta_\xi\hat{q}_{j,k}-\epsilon^{(4)}_{j,k}\Delta_\xi\nabla_\xi\Delta_\xi\hat{q}_{j,k}), \tag{7}$$

with

$$\epsilon^{(2)}_{j,k}=k_2\Delta\tau f(r_{j+1,k},\ r_{j,k},\ r_{j-1,k}),$$
$$\epsilon^{(4)}_{j,k}=\max[0,\ k_4\Delta\tau-\epsilon^{(2)}_{j,k}].$$

Typical values of the constants are $k_2=1/4$ and $k_4=1/100$ while $f(r)$ is some smooth function over the domain of interest. Similar terms are used in the ξ and ζ directions. In this work the function $f(r)$ has been taken as a simple weighted average of the variable r at three grid points, i. e.

$$f(r)=w_1\cdot r_{j+1,k}+w_2\cdot r_{j,k}+w_3\cdot r_{j-1,k}). \tag{8}$$

In the above expression r is the variable used to detect the large gradient in the flow variable such as density or pressure.

For example,

$$r_{j,k}=\frac{|\rho_{j+1,k}-2\rho_{j,k}+\rho_{j-1,k}|}{|\rho_{j+1,k}+2\rho_{j,k}+\rho_{j-1,k}|} \tag{9}$$

gives a large value near a steep density gradient region.

The coefficient $\sigma_{j,k}$ used in Eq. (7) is the spectral radius which in three dimensions is defined as $\sigma_{j,k}=|u|+a\sqrt{\xi_x^2+\xi_y^2}+|v|+a\sqrt{\eta_x^2+\eta_y^2}+|w|+a\sqrt{\zeta_x^2+\zeta_y^2}$; a sum of the spectral radii of $\hat{A}$, $\hat{B}$ and $\hat{C}$. The subscript i is omitted in Eqs. (7) to (9).

The first part of Eq. (7) is a second-difference dissipation with an exstra density gradient coefficient to increase its value near shocks and highly reacting zones. The second part is a fourth-difference dissipation where the logic to compute $\epsilon^{(4)}_{j,k}$ switches itself off when the second-difference nonlinear coefficient $\epsilon^{(2)}_{j,k}$ is larger than the constant fourth-difference coefficient. This occurs right near the shock and within the highly reacting zones.

5. Acquisition of Physical Variables

Once we have known all the physical variables at n-th time step, then RHS of Eq. (5) can be easily calculated. The conservational variables $\hat{q}$ at $(n+1)$-th time step can be calculated by inverting the block tridiagonal matrics of Eq. (5). The physical variables ρ, u, v, w, p and T must be decoded from the conservational variables $\hat{q}$ in order to proceed to the next integration step. ρ, u, v and w can be obtained directly from the conservational variables ρ, ρu, ρv, ρw. In order to decode the pressure and temperature, a table-look-up/curve-fitting procedure must be adopted.

By using the state equation (3), the pressure relation (2) can be rewritten as follows:

$$T=\frac{h}{\overline{R}}+\frac{1}{\rho\overline{R}}\ (0.5\rho V^2-e). \tag{10}$$

Since ρ, $\overline{R}$, $\overline{V}$ and e are known, the above equation can be written as

$$T=ah+b. \tag{11}$$

From the physical data we know h as a piecewise cubic spline function of temperature T

$$h=h(T). \tag{12}$$

Eqs. (11) and (12) are solved by using the Newton-Raphson method for T and h. Once the temperature and enthalpy are known, the pressure can be calculated from Eq. (2).

6. Boundary Conditions

Since the flow is symmetric about a plane passing through the velocity vector and the body axis, only one half of the flowfield is considered. There are five types of boundaries; (i) body surface, (ii) shock surface, (iii) exit flow plane, (iv) plane of symmetry and (v) the singular line encountered in this formulation.

(i) Body surface: On a rigid surface, flow tangency condition must be satisfied for an inviscid flow. This is done forcing the contravarient velocity vector perpendicular to the body surface (η=const) to zero., i. e. $V=0$, and by extrapolating the other two contravarient velocity components U and W from the respective values at the grid points immediately above the body surface. The Cartesian velocity components are then obtained from the contravarient components by using the relations

$$\begin{pmatrix} u \\ v \\ w \end{pmatrix}=J^{-1}\begin{pmatrix} (\eta_y\zeta_z-\eta_z\zeta_y) & -(\xi_y\zeta_z-\xi_z\zeta_y) & (\xi_y\eta_z-\xi_z\eta_y) \\ -(\eta_x\zeta_z-\eta_z\zeta_x) & (\xi_x\zeta_z-\xi_z\zeta_x) & -(\xi_x\eta_z-\xi_z\eta_x) \\ (\eta_x\zeta_y-\eta_y\zeta_x) & -(\xi_x\zeta_y-\xi_y\zeta_x) & (\xi_x\eta_y-\xi_y\eta_x) \end{pmatrix}\begin{pmatrix} U \\ V \\ W \end{pmatrix}. \tag{13}$$

A relation for the pressure along the body surface is obtained from the normal momentum relation

$$p_n(\eta_x^2+\eta_y^2+\eta_z^2)^{1/2}=(\xi_x\eta_x+\xi_y\eta_y+\xi_z\eta_z)\,p_\xi + (\eta_x^2+\eta_y^2+\eta_z^2)\,p_\eta+(\zeta_x\eta_x+\zeta_y\eta_y+\zeta_z\eta_z)\,p_\zeta =-\rho U(\eta_x u_\xi+\eta_y v_\xi+\eta_z w_\xi)-\rho W(\eta_x u_\zeta+\eta_y v_\zeta+\eta_z w_\zeta). \tag{14}$$

Using second-order accurate central differences in ξ and ζ directions and one-sided first-order-accurate differences in η direction, the differential form of Eq. (14) is replaced by the factored differential equation

$$(1+\Delta\eta\delta_\xi a^n)(1+\Delta\eta\delta_\zeta b^n)\,p^n =-\rho U(\eta_x u_\xi+\eta_y v_\xi+\eta_z w_\xi)-\rho W(\eta_x u_\zeta+\eta_y v_\zeta+\eta_z w_\zeta). \tag{14a}$$

With the known values of velocity components on the body surface and the extrapolated values for density, Eq. (14a) is solved for the surface pressure.

In the present formulation the thermally insulated wall condition is assumed:

$$\text{i. e.}\quad \left.\frac{\partial T}{\partial n}\right|_{wall}=0, \tag{15}$$

or

$$(\xi_x\eta_x+\xi_y\eta_y+\xi_z\eta_z)\,T_\xi+(\zeta_x\eta_x+\zeta_y\eta_y+\zeta_z\eta_z)\,T_\zeta+(\eta_x^2+\eta_y^2+\eta_z^2)\,T_\eta=0. \tag{16}$$

With this assumption, the surface temperature is deduced from the field points and the enthalpy at this temperature is obtained from Tables. Finally by solving the pressure relation (2), the energy on the wall surface is calculated.

(ii) Shock surface: The peripheral shock that separates the disturbed flow from freestream is treated as sharp discontinuity, forming a boundary. This boundary is allowed to move freely on radial rays and the movement of shock on each ray is determined by integrating

$$\frac{d}{dt}(\Delta n_s)=w_s, \tag{17}$$

where w_s is the velocity of the shock on i, k-th ray.

This moving boundary can be further explained with reference to Fig. 2. If R_s represents the radial distance of the shock from axis of symmetry, then the shock surface can be represented as $f_s=R_s(x, y, z)-R_s=0$ at a particular time. The unit outward normal to the shock surface is given by

$$\hat{n}_s=\frac{\nabla f_s}{|\nabla f_s|} \qquad \text{or} \tag{18}$$

$$\hat{n}_s=\frac{R_{sx}\hat{i}+R_{sy}\hat{j}+R_{sz}\hat{k}}{\sqrt{R_{sx}^2+R_{sy}^2+R_{sz}^2}}. \tag{19}$$

If θ is the angle that a radial ray makes with the axis of symmetry, then the unit vector in the direction of the radial ray is given by

$$\hat{r}_s = -\cos\theta\,\hat{i} + \sin\theta\cos\phi\,\hat{j} + \sin\theta\,\sin\phi\,\hat{k}, \tag{20}$$

where $\phi = \pi\zeta$.

Meanwhile a freestream velocity vector is

$$\vec{V} = |\vec{V}|\cos\alpha\,\hat{i} + |\vec{V}|\sin\alpha\,\hat{j}, \tag{21}$$

where α is the angle of attack and V is the freestream velocity. Calculations at this boundary have to be done twice during the solution process for one time step: First, before the integration process, to obtain flow variables behind the known peripheral shock and next, after the integration process, to move the shock to satisfy the new flowfield.

(a) Determination of flow variables behind a known bow shock: Once the shock locations on all radial rays are known, the unit outward normal $\hat{n}$ can be determined using Eq. (19). The shock angle with respect to the freestream velocity vector $\vec{V}$ is given by

$$\beta = \sin^{-1}\left(\frac{\vec{V}\cdot\hat{n}_s}{|\vec{V}|}\right). \tag{22}$$

The Rankine-Hugoniot shock conditions in a real gas can be written as follows:

$$h_2 = h_\infty + \frac{V_{n\infty}^2}{2}\left(1 - \frac{\rho_\infty^2}{\rho_2^2}\right), \tag{23}$$

$$p_2 = p_\infty + \rho_\infty V_{n\infty}^2\left(1 - \frac{\rho_\infty}{\rho_2}\right), \tag{24}$$

$$V_{n_2} = V_{n_\infty} - \left[(p_2 - p_\infty)\left(\frac{1}{\rho_\infty} - \frac{1}{\rho_2}\right)\right]^{1/2}, \tag{25}$$

where the subscript 2 indicates the value downstream of the shock and the subscript ∞ the freestream value. V_{n_∞} is the freestream velocity component normal to the shock wave, written as $\vec{V}\cdot\hat{n}_s$.

Eqs. (23) through (25) and the state equation (3) are to be solved iteratively to obtain the flow variables downstream of a shock. The procedure can be written as:

Step 1: Assume $\rho_2 = \rho_{2)_{\text{inviscid}}}$,

$$\rho_{2)_{\text{inviscid}}} = \rho_\infty\left\{\frac{\frac{\gamma+1}{2}M_\infty^2\sin^2\beta}{1+\frac{\gamma-1}{2}M_\infty^2\sin^2\beta}\right\}.$$

Step 2: Calculate h_2 and p_2 using Eqs. (23) and (24).

Step 3: Obtain the temperature for the enthalpy h_2 from the physical data by using table lookup procedure and Newton-Raphson's root finding method.

Step 4: Then calculate ρ_2 using the state equation (3).

Step 5: Repeat Steps 1 through 4 until convergence.

Step 6: The velocity vector behind the shock $\vec{V}_2=\vec{V}_\infty-(V_{n_\infty}-V_{n_2})\tilde{n}$ is to be calculated using Eqs. (21) and (25).

(b) Determination of shock movement: The new flowfield between the shock and body surfaces at time $(n+1)\Delta t$ can be obtained from the flowfield at time $n\Delta t$ by integrating the difference form of the governing equations. Now it is necessary to adjust the peripheral shock to match with the new flowfield. This can be done if we know the downstream pressure value. By rearranging the Rankine-Hugoniot relations, the shock velocity λ_{shock} normal to the shock and the enthalpy can be expressed as functions of the downstream pressure p_2 as follows:

$$h_2=h_\infty+0.5(p_2-p_\infty)\left(\frac{1}{\rho_2}+\frac{1}{\rho_\infty}\right), \tag{26}$$

$$\lambda_{\text{shock}}=\left[(p_2-p_\infty)\left(\frac{1}{\rho_\infty}-\frac{1}{\rho_2}\right)\right]^{1/2}-V_{n_\infty}. \tag{27}$$

The downstrem pressure p_2 can be obtained by extrapolating the pressure values at the neighboring field points. The procedure of calculating λ_{shock} can be listed as:

Step 1: Assume $\rho_2=\rho_{2)\text{extrapolated}}$.
Step 2: Calculate the temperature using the state equation (3).
Step 3: Obtain the enthalpy from the physical data (JANAF Tables).
Step 4: Then calculate ρ_2 using Eq. (26).
Step 5: Repeat Steps 1 through 4 until convergence.
Step 6: Shock velocity λ_{shock} is calculated from Eq. (27).

Once the shock velocity normal to the shock is known, the shock velocity in i, k-th ray direction can be obtained from the relation

$$w_s=\lambda_{\text{shock}}/\hat{n}_s\cdot\hat{n}_s.$$

By integrating the Eq. (17), the shock movement on each ray can be calculated.

(iii) Exit boundary condition: Since the flow across this plane is supersonic everywhere, the flow variables on this boundary are extrapolated from the upstream values.

(iv) Plane of symmetry: The grid system is chosen such that there are a pair of windward and leeward planes ($\zeta=$const) adjacent to the calculation domain across the place of symmetry. Flow variables on these planes are obtained simply by applying the reflecting image principle, i. e. all the flow variables except w are reflected symmetrically whereas w is reflected anti-symmetrically that $w=0$ on the plane of symmetry.

(v) Singular line: Though a limiting form of the governing equations is used on the singular line, the choice of a spherical body-oriented coordinate system allows us to avoid the singularity in the finite-difference formulation. This is because, on a singular line, ξ and ζ derivatives of x, y and z (e.g. $x_\xi|_J$, $y_\xi|_J$ etc.) are zero; x, y and z do not change with the change in ξ and ζ on this axis and hence $\hat{E}$ and $\hat{G}$ fluxes are identically zero on the singular line. In order to use consistent dissipative terms in ξ direction near the singular line, it is necessary to know the values of the conservational variables on the singular line. Simple extrapolation procedure is used in the present formulation. Though it is not correct to extrapolate the flow varibles on the singular line from the interior variables since

the singular line is completely immersed in subsonic flow (up to moderate angles of attack), it would not introduce significant errors because these extrapolated values are used only to calculate dissipative terms.

7. Stability and Initial Conditions

By applying linear stability analyses to the one-dimensional operators in the finite-difference scheme, Eq. (5), the stability criterion can be obtained as (7)

$$\Delta\tau=\min\left\{\frac{\Delta\xi}{\lambda_{\max}},\ \frac{\Delta\eta}{\mu_{\max}}\cdot\frac{\Delta\zeta}{\theta_{\max}}\right\},$$

where $\lambda_{\max}$, $\mu_{\max}$ and $\theta_{\max}$ are the eigenvalues of the matrices $\hat{A}$, $\hat{B}$ and $\hat{C}$, respectively. In our present analysis, calculations are started with the CFL number as high as 5. As the solution proceeds toward a steady state, the CFL number can be increased; but in most of our calculations it has been preferred to use a constant CFL number equal to 5.

In order for the peripheral shock to be fitted to the flowfield, one has to initiate the calculations by assuming an initial shock and a flowfield. All the real gas calculations are started from the perfect gas solutions.

8. Results and Discussions

The present hybrid implicit scheme is superior to generalized shock capturing methods in calculating hypervelocity flows. This is mainly because of the negligibly weak oscillations appearing in the flow variables near the shock. This method requires minimum number of grid points whereas, for generalized SCM's, grid points have to be clustered near a shock wave to obtain correct jump values, and requires appreciable number of grid points between the outer boundary and the peripheral shock, for example, within the freestream just to allow the oscillations generated in the upstream side of the shock wave. MacCormack (8) has suggested that shocks can be captured most accurately with minimum number of grid points when the coordinate mesh is aligned with the shock. Adaptive grid and floating-mesh shock-capturing methods (9) use such techniques. To show the advantages of the present method simple calculations are made with an ideal gas model. The solutions obtained with a 20×20 grid system, in the form of shock structure and Mach line contours, are shown in Fig. 3(a). The solution has converged to machine zero accuracy in less than 800 time steps, taking less than 20 sec cpu time on a Fujitsu VP-100 computer. The same calculations are repeated with a floating mesh shock capturing method. In this method shock has not been treated as discontinuity and is captured completely by the algorithm; but the mesh coordinate has been adjusted to align with the shock wave. Computed results are also shown in Fig. 3. The present method and the floating mesh SCM gave identical results while the solution has reached steady state quite rapidly in the present method. Such an oscillation-free completely-converged solution can not be obtained by the generalized shock

capturing methods at these high Mach numbers. This study suggests that special shock capturing methods such as the present one are preferable to compute hypersonic flows.

Using the present hybrid method, the flowfields over two-dimensional and three-dimensional rocket nose configurations are calculated for several Mach numbers using real gas models. Used freestream conditions are the density $\rho_\infty = 0.8728 \times 10^{-4}$ kg/cm^3, the pressure $p_\infty = 5.5$ kg/m^2 and the temperature $T_\infty = 218.36$ K. In Fig. 4 isobars, constant density lines and isothermal lines in the two-dimensional flowfields are shown for the freestream Mach numbers 15 and 25, where a 100×40 grid system having clustered grid points near the shock and body is used. The expansion fan emanating from the shoulder portion is clearly visible in the figure. Computed shock structures are very smooth; the present method does not pose any difficulty even if the shock wave weakens.

The pressure, density and temperature distributions along the stagnation line for three Mach numbers are plotted in Fig. 5. Absolutely oscillation-free distributions can be seen. For the same freestream conditions a perfect gas would give $p/p_\infty = 575.42$, $\rho/\rho_\infty = 6.4259$ and $T = 27319.2$ K at the stagnation point at a Mach number 25. Due to the real gas behavior, T has been dropped by 29.7 percent and hence the density increased by 40.1 percent whereas the pressure did not change. Shock standoff distance has been reduced by 27.33%. For $M_\infty = 20$, the convergence history is shown in Fig. 5(b). The residual has become less than 10^{-10} within 2000 steps for which a Fujitsu VP-200 computer takes 450 sec.

Similar caluculations are made on an axisymmetric body at angles of attack (Fig. 6). Computed isobars and isothermal lines in the plane of symmetry are for $M_\infty = 20$ at angles of attack 0, 5° and 10°. For these calculations a $40 \times 20 \times 20$ grid system has been used and the steady state is reached in less than 1500 steps. The isothermal lines in flows around an axisymmetric body are very much different from those on two-dimensional bodies. In flows around an axisymmetric body, all the isothermal lines approach tangent to the body. This is because of a thin entropy layer that exists only in the flows around axisymmetric bodies.

9. Conclusions

Through a variety of calculations on two-dimensional and three-dimensional bodies flying at the Mach numbers ranging between 15 and 25, the present analysis proved to be efficient and accurate in calculating hypersonic flows around rocket geometries. It is efficient because of its minimal requirement on grid points. It is more accurate compared to general shock capturing methods because the strongest shock in the flow is treated exactly. The boundary treatment of a shock wave shows excellent matching with the implicit Beam-Warming scheme; as a result calculations are started with the CFL number as high as 5. This combination of shock fitting and implicit approach would provide a powerfull tool to handle chemically reacting flows.

Aknowledgement

This work was supported partly by the Science Research Fund of Ministry of Education and Culture (General Research Category C No. 60550039, 1984-1986), by Drs. T. Ogawa and T. Ishiguro, the Computer Center of National Aerospace Laboratory, Tokyo, and by Profs. H. Oguchi and T. Abe, ISAS (Institute of Space and Astronautical Sciences) regarding AOTV project.

References

1) Thomas, P. D., Vinokur, M., Bastianon, R. and Conti, R. J., Numerical Solution for the Three-Dimensional Inviscid Supersonic Flow, AIAA Journal, Vol. 10, No. 7, July 1972.
2) Kutler, P., Reinhardt, W. A. and Warming, R. F., Multishocked, Three-Dimensional Supersonic Flowfields with Real Gas Effects, AIAA Journal, Vol. 11, No. 5, May 1973.
3) Beam, R. and Warming, R. F., An Implicit Factored Scheme for the Compressible Navier-Stokes Equations, AIAA Paper No. 77-645, June 1977.
4) Pulliam, T. H. and Steger, J. L., Implicit Finite-Difference Simulation of Three-Dimensional Compressible Flow. AIAA Journal, Vol. 18, No. 2, Feb. 1980.
5) JANAF Thermochemical Tables, NSRDS, 1971.
6) Pulliam, T. H., Artificial Dissipation Models For the Euler Equations, AIAA Paper No. 85-0438, Jan. 1985.
7) Wang, Y. Y. and Fujiwara, T., Numerical Analysis of Transonic Flow around a Two-Dimensional Airfoil by Solving Full Navier-Stokes Equations, Memoirs of the Faculty of Engineering, Nagoya University, Vol. 36, No. 2, pp. 138-178, 1984.
8) MacCormack, R. W. and Paullay, A. J., The Influence of the Computational Mesh on Accuracy for Initial Value Problems with Discontinuous or Non-Unique Solutions, Computers and Fluids, Vol. 2, pp. 339-361, 1974.
9) Rizzi, A. W. and Inouye, M., Time-Split Finite-Volume Method for Three-Dimensional Blunt-Body Flow, AIAA Journal, Vol. 11, No. 11, pp. 1478-1485, 1973.

Appendix

$\hat{A}^n$, $\hat{B}^n$, and $\hat{C}^n$ in Eq. (5) are the Jacobian Matrices obtained in the time linearization of $\hat{E}^n$, $\hat{F}^n$ and $\hat{G}^n$, respectively,

$$\text{i.e. } \hat{A}^n=\frac{\partial \hat{E}}{\partial \hat{q}},\ \hat{B}^n=\frac{\partial \hat{F}}{\partial \hat{q}},\ \hat{C}^n=\frac{\partial \hat{G}}{\partial \hat{q}}$$

After performing differentiation on each term, $\hat{A}^n$, $\hat{B}^n$, and $\hat{C}^n$ can be written as follows:

$\hat{A}^n$, $\hat{B}^n$ or $\hat{C}^n=$

$$\begin{pmatrix} K_0 & K_x & K_y & K_z & 0 \\ -u\theta+K_x\Psi & \theta+uK_x(1+1/\varepsilon)+K_0 & K_yu+K_xv & K_zu+K_xw & -K_x/\varepsilon \\ -v\theta+K_y\Psi & K_xv+K_yu & \theta+vK_y(1+1/\varepsilon)+K_0 & K_zv+K_yw & -K_y/\varepsilon \\ -w\theta+K_z\Psi & K_xw+K_zu & K_yw+K_zv & \theta+wK_z(1+1/\varepsilon)+K_0 & -K_z/\varepsilon \\ \theta\Psi-(e+p)\theta & K_x(e+p)+\theta u/\varepsilon & K_y(e+p)+\theta v/\varepsilon & K_z(e+p)+\theta w/\varepsilon & \theta(1-1/\varepsilon)+K_0 \end{pmatrix},$$

where

$$\theta=K_xu+K_yv+K_zw\ ;\ \varepsilon=1-c_p/\overline{R}\ ;\ \overline{R}=\frac{R_0}{M}\ ;\ M=\frac{1}{f/M_{N_2}+(1-f)/M_{O_2}};$$

$$f=\frac{\rho_{N_2\infty}}{\rho_\infty}\ ;\ \Psi=\frac{1}{\varepsilon}[h-c_pT+0.5(u^2+v^2+w^2)].$$

To obtain $\hat{A}^n$, set $K_0=\xi_t$, $K_x=\xi_x$, $K_y=\xi_y$, $K_z=\xi_z$, and

to obtain $\hat{B}^n$, set $K_0=\eta_t$, $K_x=\eta_x$, $K_y=\eta_y$, $K_z=\eta_z$, and

to obtais $\hat{C}^n$, set $K_0\zeta_t$, $K_x=\zeta_x$, $K_y=\zeta_y$, $K_z=\zeta_z$.

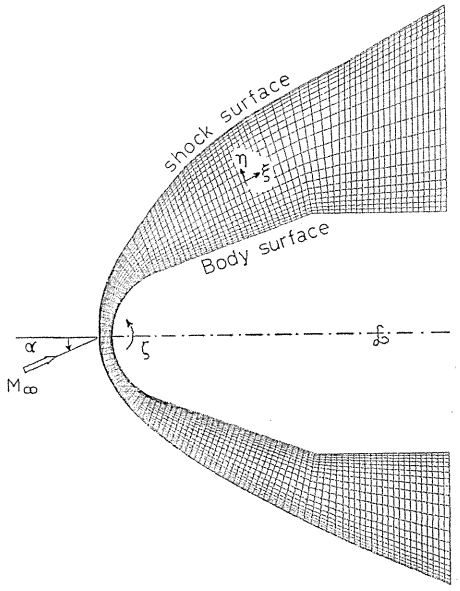

Fig. 1. Body Geometry and the Moving Grid System.

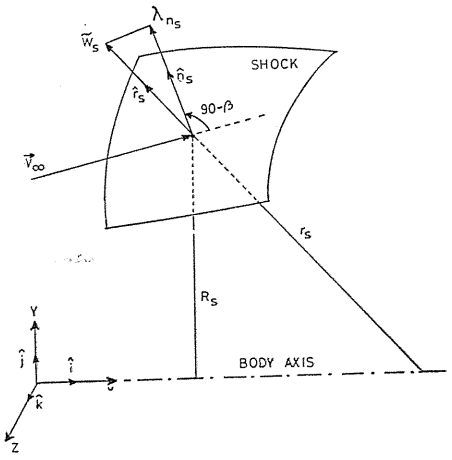

Fig. 2. Geometry for Shock Velocity Evaluation.

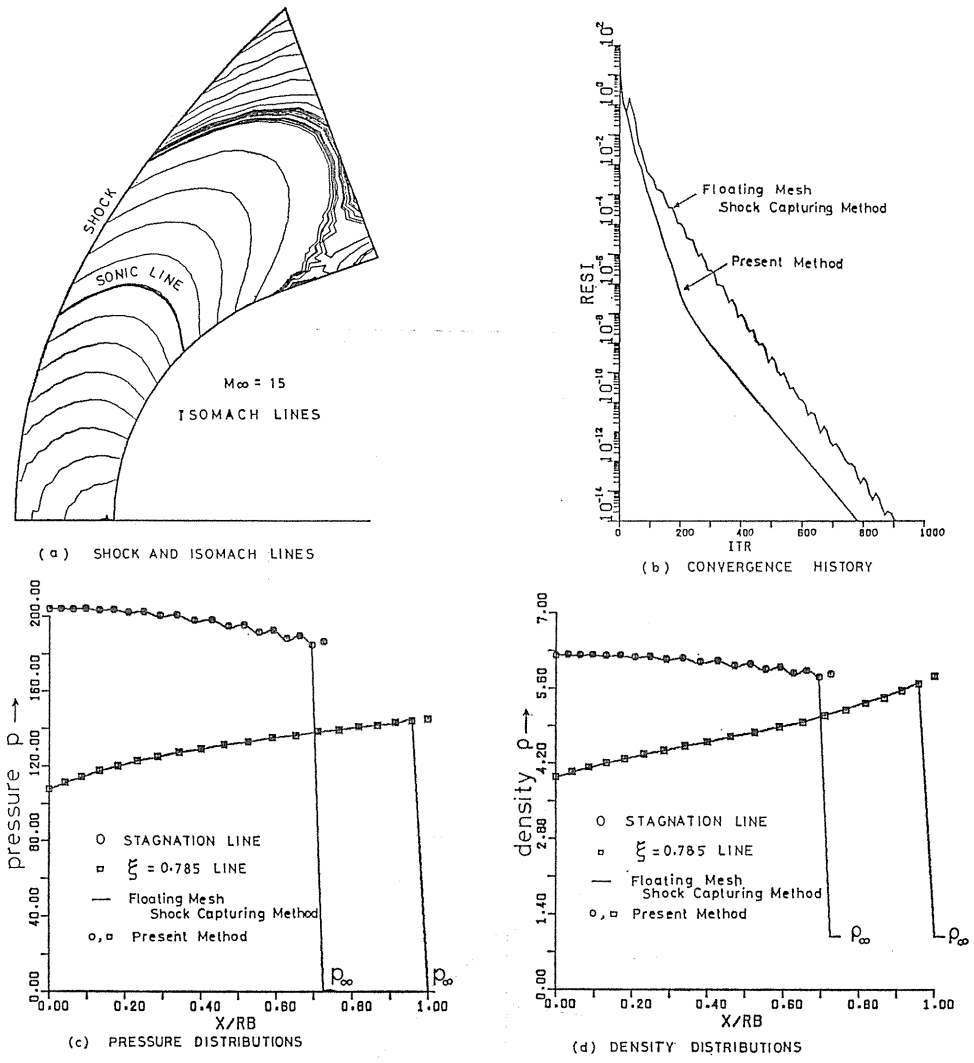

Fig. 3. Comparison of Solutions Obtained Using Present Method and Floating Mesh Shock Capturing Method for $M_\infty=15$.

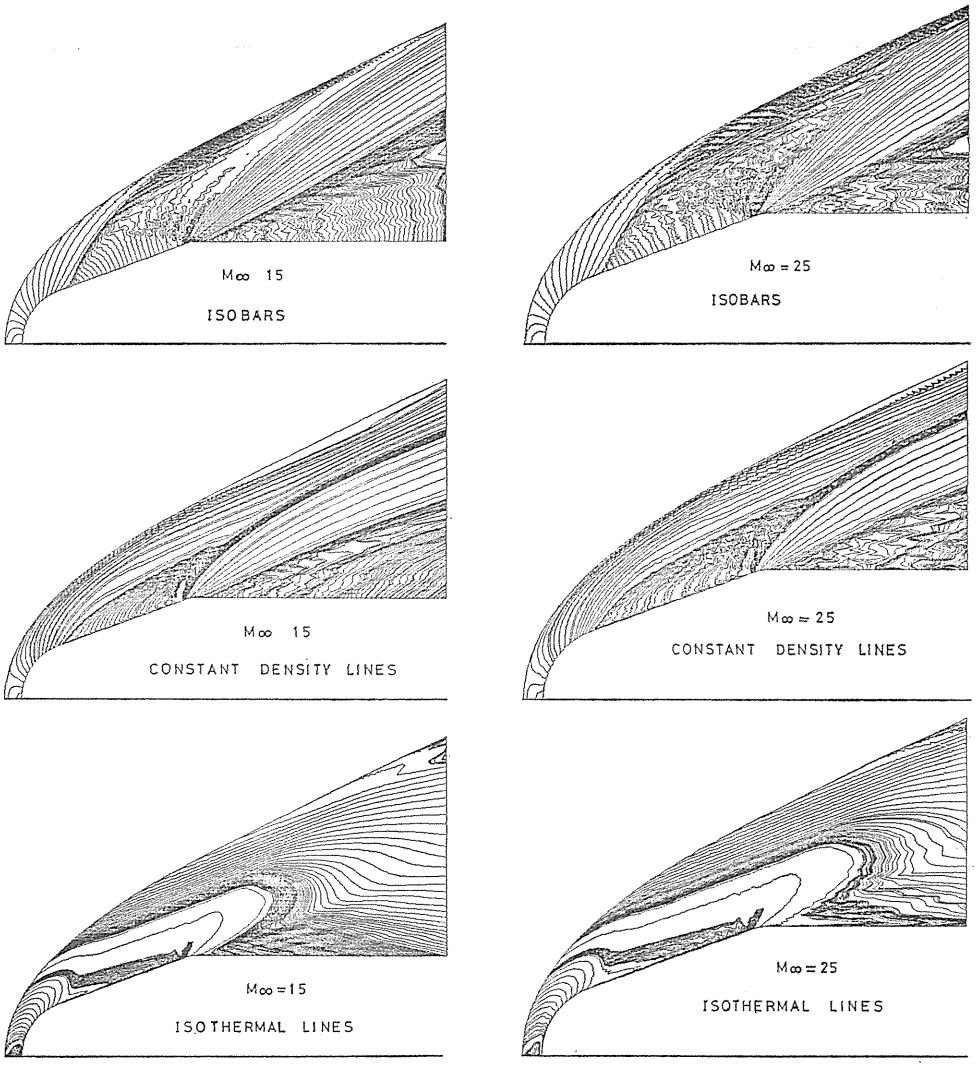

Fig. 4. Isobars, Constant Density and Isothermal Lines for M_∞=15 and 25.

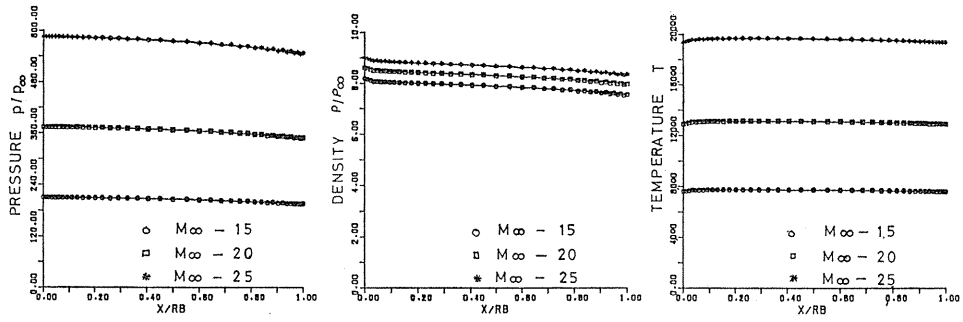

Fig. 5. (a) Pressure, Density, and Temperature Distributions along Stagnation Line for M_∞=15, 20 and 25.

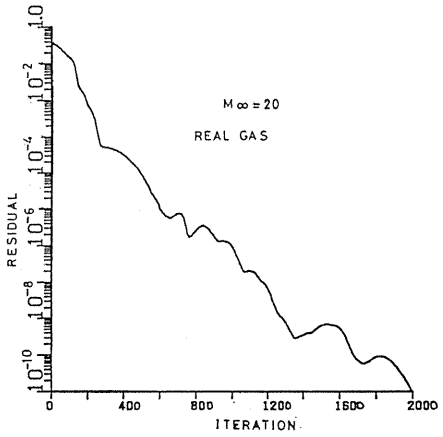

Fig. 5. (b) Convergence History for M_∞=20 Calculation.

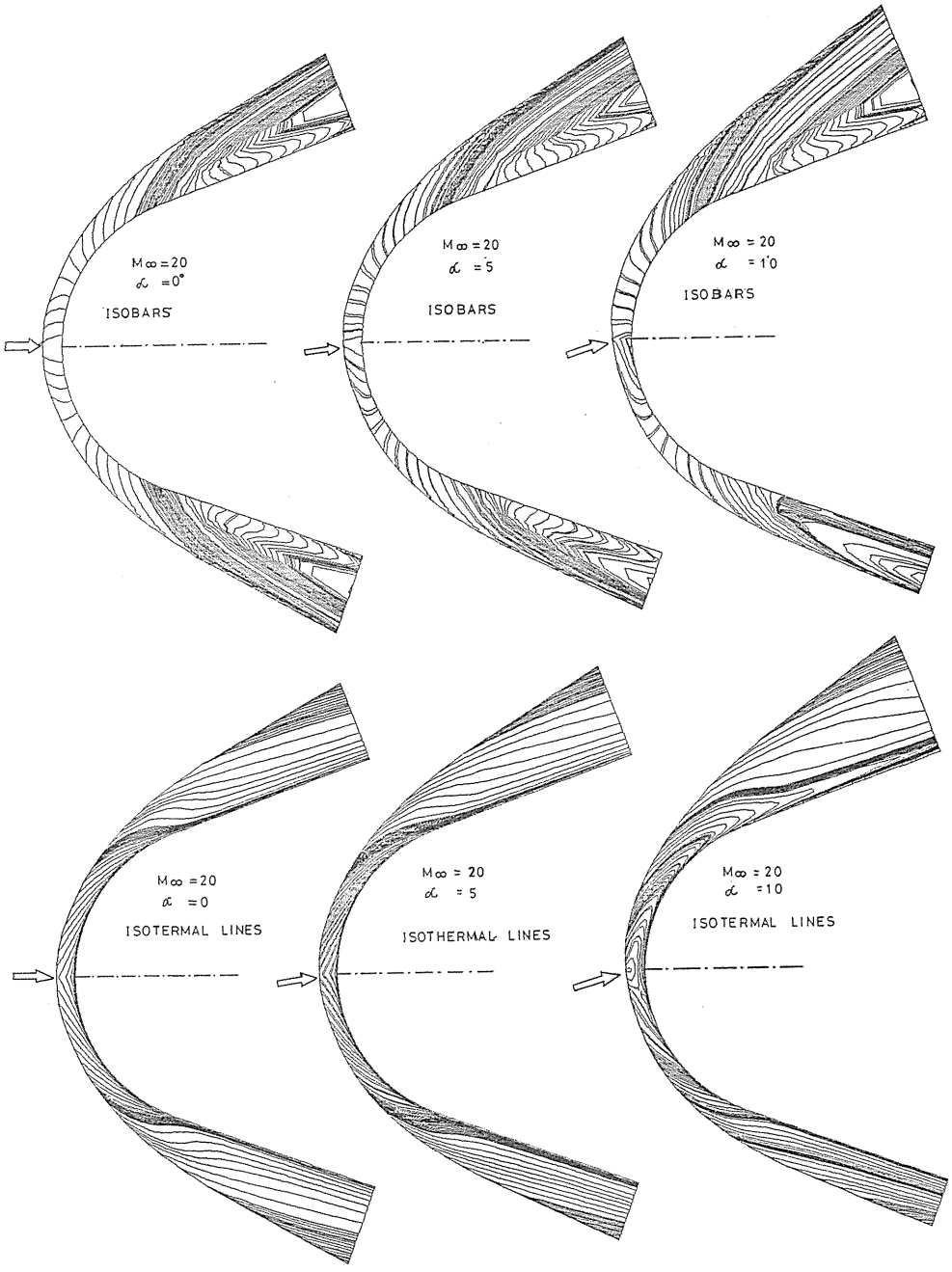

Fig. 6. Isobars and Isothermal Lines in the Flow over Axisymmetric Body at Angles of Attack.